THE INTERACTING SYSTEM NGC 7753–7752 (ARP 86). II. N-BODY MODELING

HEIKKI SALO

Department of Astronomy, University of Oulu, SF-90570 Oulu, Finland

AND

EIJA LAURIKAINEN

Tuorla Observatory, University of Turku, SF-21500 Piikkiö, Finland

ABSTRACT

The interacting disk galaxy pair NGC 7753–7752 (Arp 86) is studied in terms of three-dimensional N-body simulations and compared with CCD observations (Laurikainen, Salo, & Aparicio 1993). The numerical code is based on the use of overlapping, comoving spherical polar potential grids combined with Cartesian integration, and both members are described with self-gravitating star + gas disks embedded in analytical spherical halos. Obtained models match the morphology and velocity field of the main tidal features as well as give correct projected separation and radial velocity difference between the components. The models suggest that the components of Arp 86 are moving in a low-inclination ($i \approx 20°$), low-eccentricity ($\epsilon \approx 0.15$) relative orbit, most probably resulting from dynamical friction. This orbital geometry favors material transfer between the components, which is proposed as the cause of the anomalously large activity of the companion. About 5% of the large galaxy gas mass is estimated to have been transferred to the companion.

Subject headings: galaxies: individual (NGC 7753–7752) — galaxies: interactions — galaxies: spiral — methods: numerical

1. INTRODUCTION

Several statistical surveys of large samples of close galaxy pairs (e.g., Dahari 1984, 1985; Kennicutt & Keel 1984; Joseph & Wright 1985; Cutri & McAlary 1985; Bushouse 1987) as well as detailed studies of individual strongly interacting systems suggest a connection between tidal encounters and starbursts as well as nuclear activity. Schombert, Wallin, & Struck-Marcell (1990) indicated that star formation can be induced also in the weak tidal features. However, the correlations are not simple: for example, there seems to be no clear dependence between the apparent separation of the components and the activity shown by them. Not even all pairs with clear morphological tidal features exhibit excess activity, whereas signs of increased activity can be observed in samples extending to large mutual separations (Laurikainen & Moles 1989). This implies that the influence of tidal encounters must depend on several factors, probably including, besides the strength and geometry of perturbation, the initial dynamical state of the galaxy as well as the amount of gas and its preencounter distribution. Also, mass transfers between components might sometimes be significant. In addition, the observed levels and sites of activity most probably depend on the phase of the tidal perturbation (see Wallin 1990).

The large number of free parameters indicates that statistical approaches, although extremely important, can have only limited success in describing the effects of interactions. Ideally, one should study in detail a large number of interacting pairs representing various phases and types of interaction and, based on this sample, study the general effects of interactions. This kind of observing program, concentrating on systems with relatively weak perturbations, has been started with the Nordic Optical Telescope, combining $BVRI$ photometry and spectroscopic observations, the results being interpreted by comparison with N-body simulations. Somewhat similar programs are carried out by other groups (see, e.g., Smith & Wallin 1992),

based however on different selection criteria, observation techniques, and modeling methods. In the present study, self-gravitating simulation models for the system Arp 86 (NGC 7753–7752) are presented and compared with our CCD observations (Laurikainen, Salo, & Aparicio 1993, hereafter Paper I).

The system Arp 86 consists of a grand-design SAB(rs)bc or SAB(rs)b spiral, NGC 7753, and an irregular compact companion NGC 7752. With the companion located at the end of an extended spiral arm, the overall morphology is very reminiscent of the M51 system. Despite its relatively small angular size (the angular size of the larger system is about one-fourth that of M51), the system is quite well studied. For example, Marcelin et al. (1987) have presented detailed velocity fields and rotation curves, based on interferometric Hα observations. In Paper I deep $BVRI$ CCD images were analyzed, and detailed color index maps were derived. In addition. Laurikainen & Moles (1989) studied this system by long-slit spectroscopy and estimated the total Hα fluxes. Perhaps the most interesting feature of the system is the high activity level shown by the companion: as noted in Paper I, its total 10 μm IR flux (Joseph et al. 1984) as well as its Hα flux are among the largest measured for any interacting or starburst galaxy. In fact, they are close to the levels typically found only in merging systems (Wright et al. 1988). The morphology in the B band as well as the Hα distribution suggest that the activity originates in an extended region and is thus not due to any nuclear source. An intriguing possible explanation for the observed activity, addressed in the present study, is a material transfer between the systems.

Due to its interesting observational characteristics, combined with relatively clear morphology, the Arp 86 system offers an ideal candidate for detailed simulation modeling. The main disk shows well-defined tidal bridge and tail features, connecting smoothly to the strong inner spiral structure. From

586

CCD observations, the inclination of the disk can be fairly accurately estimated and, combined with the velocity information, provides a reliable estimate for the rotation amplitude. In spite of the knotty central brightness structure, the overall light distribution of the companion also follows an exponential profile, and the velocity field shows regular disk rotation. Because the velocity fields of both systems have been measured simultaneously (Marcelin et al. 1987), the radial velocity difference is known with great accuracy. Therefore, simulation models should be fairly well constrained by various observations.

In this study, numerical simulations performed with a three-dimensional multiple spherical polar grid simulation code are presented. The main ingredients of the code, as well as the orbital search procedures, are presented in § 2, while § 3 describes the results of simulation modeling of Arp 86. First, the factors affecting the choice of initial models are discussed, and a brief survey of the morphological effects of various orbital parameters is presented. After a good orbital model is found, more detailed experiments including a dissipative gas component are studied. As convincing evidence for an almost circular, near-planar orbit is found, we also study the long-term influence of such extended perturbation. Especially as mass transfer to the companion is inferred from the models, we concentrate on studying whether it might have significant influence on the companion.

2. SIMULATION MODELING

The goal of our N-body modeling is to derive knowledge about the orbital history of the components of NGC 7753–7752, in order to estimate the duration and strength of the tidal forces experienced by the systems. Constraints for the models are obtained from the morphology and velocity field of the tidal features, as well as from the requirement that the observed separation of the components and the radial velocity difference must be reproduced as accurately as possible. In this section we briefly describe our N-body method and the procedures for matching the geometrical constraints of the relative orbit. A more detailed description of the code will be published separately (Salo 1993).

2.1. Simulation Method

In order to study the influence of various orbital parameters on the morphological features induced by tidal interaction and to match them to observations of a specific system, a large number of trial simulations is required. This implies the need for a fast N-body method. In general, polar grid codes offer efficient means for the evaluation of disk self-gravity, and give good spatial resolution in the dense inner parts of the system. However, single-grid methods are clearly not suitable if two interacting components are to be studied simultaneously, in which case Cartesian potential grids are usually employed. Cartesian coordinates also simplify the orbital integrations as well as the application of fast Fourier transforms (FFTs), but, on the other hand, they lead to rather poor spatial resolution, since both components have to be covered by fixed-size cells. Therefore two-dimensional multiple polar grid code was recently developed (Salo 1991), combining the advantages of both polar potential evaluation and Cartesian integration. The method was based on the use of mutually overlapping logarithmic polar potential grids, comoving with the halo centers of the components and thus giving good resolution simultaneously for both components. Moreover, polar grids were used

only for potential evaluation, while orbital integrations were carried out in the center-of-mass rectangular coordinate system, thus allowing the use of fast Cartesian leapfrog integration. This code was later extended to three dimensions (Salo 1993; see also Salo & Byrd 1990) by replacing polar grids with spherical polar grids. All the simulations of the present study are performed with this improved method, since it allows much more realistic modeling of individual observed systems with mutually tilted disks on inclined relative orbits.

In the code the individual galaxies are represented with self-gravitating disks embedded in analytically described spherical halos. In the present experiments we apply truncated exponential disks for the self-gravitating components and singular isothermal sphere models for the analytical halos. Disk self-gravity is calculated with the help of logarithmic spherical polar grids, centered at each moving halo, and aligned with the initial, mutually tilted disk planes. The mass of each particle is assigned to the grid of the system it initially belonged to, and the spherical force components are calculated by interpolation from potential grids. As the grids overlap, forces from both systems are available at each particle location and can be transformed to a rectangular center-of-mass coordinate system and added together. Forces due to halos are calculated directly, from analytical halo radial force functions. Forces on halos are calculated similarly to forces on particles, which implies that halo deformations are not taken into account. Integrations, for both particles and halos, are carried out with the explicit time-centered leapfrog in Cartesian coordinates. Notice that in the case of a point-mass perturber the use of moving halos is totally equivalent to the treatment in single-grid codes where the origin is fixed to the main galaxy and both direct and indirect forces are considered.

Typically, $N_\phi = 36$ azimuthal, $N_R = 36$ radial, and $N_\theta = 19$ latitudinal density cells are used for each grid (implying 10° resolution). The calculation of mutual gravitational potential between the "floating azimuthal rings" ($R =$ constant, $\theta =$ constant) is performed with FFT, after which contributions from different radii and latitudes are added together. The main restriction for the resolution is set by the memory limitations, since the calculation of potential implies pretabulation of the Fourier transform of inverse distance between the calculation cells, so that the required memory scales proportionally to $N_R^2 N_\theta^2 N_\phi$. Because of limited memory and number of cells, it is advantageous to use unequal latitudinal grid spacings and increase the latitude resolution near the equatorial planes. Numerical tests indicate that errors in the forces interpolated from the grid are a few percent at most. Also, conservation of energy and angular momentum is in all models better than 1%.

In addition to stellar populations, gas is also included in terms of dissipatively colliding particles (Salo 1991). Instead of using collision grid methods (e.g., Combes & Gerin 1985; see also Elmegreen et al. 1992; Thomasson 1987), times and locations of impacts between finite-sized particles are evaluated with the full accuracy provided by the orbital integrations, thereby providing good resolution of gas compression regions. In this respect, the method of collisional calculations is very similar to those usually employed in planetary ring simulations (e.g., Salo 1987, 1992; Wisdom & Tremaine 1989). Notice that, as both galaxies can contain dissipative particles, shocks due to overlap of two interacting gas disks can also be modeled.

The change of the relative velocity in a cloud-cloud impact is modeled in terms of two parameters, α and β, describing the change of the component of relative velocity in the perpendicu-

lar and tangential direction with respect to the tangent plane of impact. For example, $\alpha = 1$ corresponds to perfectly elastic impact, and $\alpha = 0$ to totally inelastic impact. In the case of $\beta = 0$ there is no friction, while $\beta = 1$ corresponds to the case where the tangential velocity difference is completely lost in impact. Individual changes are determined by the conservation of linear impulse. Thus

$$\Delta V_1 = -\frac{\mu_2}{\mu_1}\Delta V_2 = \frac{\mu_2}{\mu_2 + \mu_1}[(1 + \alpha)V_{\mathrm{rel}}\cdot CC$$
$$+ \beta C \times (V_{\mathrm{rel}} \times C)]\,, \quad (1)$$

where $C = (R_2 - R_1)/(\sigma_1 + \sigma_2)$ is the unit vector in the direction joining the centers of colliding particles, while σ_1, σ_2, μ_1, and μ_2 stand for their radii and masses, respectively, and $V_{\mathrm{rel}} = V_2 - V_1$ for the precollisional relative velocity (Salo 1987).

Alternatively, collisions between gas particles can also be ignored; gas is thus treated as another stellar component, having, for example, different initial random velocity dispersion as compared with star particles. This enables fast two-component simulations where short-term evolutionary differences between stellar and gaseous components are examined by describing the latter with initially cold disk with Toomre parameter $Q_{\mathrm{T}} = 0$ (see Sundelius et al. 1987).

A simple model for tracing star formation regions is also included, by creating ballistically moving test particles (representing newborn stellar associations, denoted by OB particles) in a certain fraction of gas cloud impacts (see Roberts & Haussman 1984; Noguchi 1988) and following their spatial and temporal distributions. This crude and possibly grossly misleading inclusion of astrophysical processes should not be taken too literally. Rather, OB particles can be considered as a convenient way of keeping track of the regions where gas compression predominantly takes place. Since the impact probability scales proportionally to the square of gas surface density, this mimics the Schmidt law of star formation. As demonstrated by Larson (1988), several possible accretional mechanisms for the formation of massive molecular cloud complexes might lead to approximately the same type of proportionality between star formation rate and gas density.

2.2. Method of Orbit Fitting

In order to compare the observed morphological features with simulation results, the orientation and scale of the simulation coordinate system with respect to the sky coordinates must first be established. We take the simulation xy plane to be aligned with the plane of the main disk, with the x-axis pointing to the descending node of the disk with respect to the sky plane. After fixing the length of the simulation radius unit in arcseconds, r_{sca}, and the simulation velocity unit in kilometers per second, v_{sca}, the measured position angle (P.A.) and inclination i can be used to project the simulation coordinates and velocities $(x_s, y_s, z_s; \dot{x}_s, \dot{y}_s, \dot{z}_s)$ to sky position $(x_{\mathrm{sky}}, y_{\mathrm{sky}})$ and radial velocity difference (v_{rad}):

$$x_{\mathrm{sky}} = r_{\mathrm{sca}}(-x_s \sin \mathrm{P.A.} - y_s \cos i \cos \mathrm{P.A.}$$
$$- z_s \sin i \cos \mathrm{P.A.})\,,$$
$$y_{\mathrm{sky}} = r_{\mathrm{sca}}(x_s \cos \mathrm{P.A.} - y_s \cos i \sin \mathrm{P.A.} \quad (2)$$
$$- z_s \sin i \sin \mathrm{P.A.})\,,$$
$$v_{\mathrm{rad}} = v_{\mathrm{sca}}(\dot{y}_s \sin i + \dot{z}_s \cos i)\,.$$

Here x_{sky}, y_{sky} refer to a rectangular sky coordinate system with x-axis pointing to the west and y-axis to the north, centered at the nucleus of the main system, and v_{rad} is counted as positive toward the observer. Correspondingly, $x_s, y_s, z_s; \dot{x}_s, \dot{y}_s, \dot{z}_s$ are calculated with respect to the halo center of the main component. Written for the relative coordinates of halo centers in simulations, equations (2) define three constraints set by the observed separation and velocity difference between the components, which must be fulfilled by any acceptable model. Also, we can trace from observations the main tidal features and compare them directly with the projected outlook of the simulation system as seen from our viewing direction.

Since only two components of true separation between the systems and one component of velocity difference are known, three additional parameters must be given in order that the relative orbit be determined. There are several possible ways of choosing these. The most obvious one would be to guess the present separation of the systems in the direction perpendicular to the sky plane, as well as the two unknown velocity components parallel to the sky plane. The orbit could then be followed backward by assuming some reasonable analytical mass distribution for the systems, and the actual N-body experiment would be started from some point along this past orbit. The best orbit would then correspond to the one producing the closest match to the observed morphology at the present time. This is the procedure adopted by, for example, Engström & Athanassoula (1991) in their M51 orbit fittings. However, in the present study a different approach has been chosen: we vary the azimuth (AZI, measured counterclockwise along the disk from the x-axis) and distance (R_{cross}) of the previous disk-plane crossing (corresponding to three free parameters of the orbit), as well as the time (T_{obs}) it has taken for the companion to reach its present position (counted from the disk-plane crossing), and continue the search until good morphological agreement is found. This set (R_{cross}, AZI, T_{obs} plus constraints for present separation and velocity difference) also defines a unique orbit in the given mass distribution, and can be found by iterative methods. This set is especially useful in the case of inclined passages, since the strongest deformations are induced near the disk-plane crossing: for the special case of almost planar orbits, the azimuth and separation at the pericenter would be a more appropriate choice of free parameters. It is clear that most combinations of R_{cross}, AZI, and T_{obs} are excluded, as they do not allow any orbit fulfilling the observational constraints.

In practice the iteration is performed by minimizing with the Powell method the sum of squares

$$\Delta^2 = \left(\frac{x_{\mathrm{sky}} - x_{\mathrm{obs}}}{r_{\mathrm{sca}}}\right)^2 + \left(\frac{y_{\mathrm{sky}} - y_{\mathrm{obs}}}{r_{\mathrm{sca}}}\right)^2 + \left(\frac{v_{\mathrm{rad}} - v_{\mathrm{obs}}}{v_{\mathrm{sca}}}\right)^2\,, \quad (3)$$

where x_{sky}, y_{sky}, and v_{rad} are the projected separation and velocity difference between the components obtained from the trial orbit, while x_{obs}, y_{obs}, v_{obs} denote the corresponding observed quantities (scaled to simulation units, as both separations and velocity difference are then of the order of unity): integration of each trial orbit corresponds to one function evaluation in Powell's method. In general, if orbit is possible, iteration converges very fast. After this, an N-body run with self-gravitating particles can be performed. The advantage of the present method is that the fitting parameters, R_{cross}, AZI, and T_{obs}, each have a clear geometrical meaning and can be at least crudely estimated by inspecting the main morphological

features, as well as being easily adjusted according to the differences between the simulated and observed features (see § 3).

There is one drawback in the above-described search of possible orbits: due to the inclusion of gravitating disks, final positions in N-body runs can deviate significantly from those produced by trial runs where just the spherical mass distribution is taken into account. This would make the survey of the effects of various parameters in N-body runs quite difficult, as they would each lead to a somewhat different present location, making it hard to separate the effect of, for example, R_{cross} from the spurious changes caused by the variable success of fitting the observed location. However, two refinements can significantly improve the accuracy of the fitted position. First of all, instead of using a spherical halo model in orbit iterations, we can replace the potential of the main component by a combination of spherical halo model and fixed disk potential, calculated from the initial, axisymmetric disk model. This will quite efficiently reproduce the precession of the relative orbit caused by the nonspherical mass distribution, and improve essentially the agreement with self-gravitating runs. But even then the deformation of the disk during an actual N-body run can cause deviations, especially if the perturbation is strong. In order to reduce this, another iteration schema is employed, involving trial runs with self-gravity included: while performing an N-body experiment (with small particle number), we follow the orbits of several fictitious massless companion halo centers, starting with initial values slightly different from those of the actual companion, feeling the deformation caused in the primary disk by the actual companion. Initial values of the relative orbit can then be modified in the direction minimizing the difference Δ^2.

Remaining differences in the fit are usually rather small, of the order of a few percent in separation and velocity difference. Better accuracy would be meaningless, taking into account the overall crudeness of the N-body models as well as the observational uncertainty—for example, in the disk orientations.

Compared with other investigations where individual observed pairs are modeled with three-dimensional simulations, both our numerical method and our orbital search strategy are different. For example, in their recent study of the NGC 7714/7715 (Arp 284) system, Smith & Wallin (1992) use massless test particles around softened point-mass halos, and study the influence of various parameters in a manner similar to that of Toomre & Toomre (1972), without matching the exact radial velocity difference. On the other hand, Borne & Richstone (1991) apply a multiple three-body algorithm to model the NGC 7252 (Arp 226) system. In their method the disks' self-gravity is ignored, but the forces exerted by particles on the halos are included, thus allowing for evolution of the relative orbit between halos. They perform a very systematic survey through the orbital and initial orientation parameter space, to match both the complicated morphology and the rotation curve information.

Compared with Arp 86, both the above-mentioned systems represent strongly perturbed merging pairs for which accurate determination of initial parameters is very difficult, and therefore test particle methods where gross tidal features can be studied are sufficient. For Arp 86, regular morphology requires both the inclusion of disk self-gravity and accurate matching of velocity difference, in order to distinguish between various possible solutions (see below). Also, the N-body method is needed to study the long-term orbital evolution. In principle, a tree code (Barnes & Hut 1986) makes realistic modeling of true

disk/halo systems possible. For example, Barnes (1988) has applied this method to NGC 4038/4039 (Antennae), and was very successful in reproducing the simultaneous appearance of long tidal tails and an advanced merging state of the components. However, compared with our potential-grid–based method, tree codes are considerably slower and thus hard to apply to extended parameter surveys needed in matching observations of individual pairs (see, e.g., Hernquist 1990).

3. SIMULATION RESULTS

In this section the results of our numerical models are presented. In addition to displaying models leading to a relatively good fit with the observed features, the effects of varying orbital parameters are explored. The behavior of gaseous components is also studied, as well as the evolution of the companion and the long-term history of the system.

3.1. Choice of Initial Galaxy Models

In order to model the morphological deformations due to interaction, a reasonable representation for the initial nonperturbed systems must be found. This includes estimating the mass distributions of the disks, as well as rotation curves and the distribution of halo material. Since the maximum rotation amplitude is strongly dependent on the inclinations assigned to the systems, we must first address the orientations of the systems relative to our viewing direction.

3.1.1. Disk Orientations

Although the interaction is likely to warp the outer parts of the components, the inner disks should more or less retain their initial orientations. In their study of the Arp 86 velocity field, Marcelin et al. (1987) adopt inclination $i = 52°$ and position angle P.A. = 53° for the disk of NGC 7753. This position angle is used here, but for inclination we adopted the revised value of 40° determined in Paper I. For the simulation models, we also need to estimate the orientation of the companion disk with respect to the main system. Taking the Marcelin et al. values of $i = 55°$ and P.A. = 105° for NGC 7752, two possible orientations with respect to the main disk are in principle possible. Since we can assume that the spirals of the main system are trailing, its northern side is closer to us (see Fig. 5, displaying the observed velocity field). Assuming the same with the companion, we obtain $i_{rel} = 40°$, $\Omega_{rel} = 92°$, where Ω_{rel} is measured along the plane of the primary, from its nodal line with respect to the sky plane (this orientation is denoted by $ori = 1$ in § 3.7). On the other hand, assuming that the southern edge of the companion is closer to us ($ori = 2$), systems would have much higher relative inclination, $i_{rel} = 83°$, and $\Omega_{rel} = 41°$. Because the eastern edge of the companion is receding from us, the former orientation corresponds to the spin vector pointing toward us, while for the latter orientation the spin is opposite. Therefore, in the former case both systems are rotating in approximately the same sense. Later we will inspect both possible orientations separately and determine the most probable one.

3.1.2. Disk and Halo Models

The systems are modeled with truncated exponential disks, embedded in truncated singular isothermal halos. Therefore, the disk surface density is described by

$$\Sigma = \begin{cases} \Sigma_0 \exp(-R/R_e), & R \leq R_d, \\ 0, & R > R_d, \end{cases} \tag{4}$$

where R_e is the exponential scale length and R_d is the disk truncation radius. The constant Σ_0 is related to the total mass contained within R_d:

$$M_{disk} = 2\pi\Sigma_0 R_e^2 [1 - (1 + R_d/R_e) \exp(-R_d/R_e)] .$$

In Paper I the exponential scale lengths were found to be $R_e \approx 20''$ for the main disk and $R_e \approx 4''$ for the companion. For the truncation radii we initially choose $R_d = 5R_e$, which approximately gives the optical diameters at the present time. Initially all particles are distributed in the equatorial plane.

For the spherical halo, the density model (see Hunter, Ball, & Gottesman 1984)

$$\rho(R) = \begin{cases} \rho_c , & R \leq R_c , \\ \rho_c(R_c/R)^2 , & R_c < R < R_H , \\ 0 , & R_H \leq R \end{cases} \qquad (5)$$

is assumed, where R_c and R_H are the core and halo truncation radii, respectively. The total mass of the halo is given by $M_{halo} = M_c(3R_H/R_c - 2)$, where $M_c = 4\pi\rho_c R_c^3/3$ is the mass within a constant-density core. The choice of this model is based on its simplicity, as well as on the fact that it gives the main features of most observed rotation curves: inside R_c it yields a linearly rising rotation curve, which then turns flat between R_c and R_H, outside which Keplerian rotation is obtained. The appropriate parameter value for R_c can be deduced from the rotation curve once the contribution of the disk is taken into account, whereas the value of R_H is very uncertain, since the extent of massive halos is unknown.

Figure 1 displays the combined rotation curves due to the above disk and halo models, for various values of M_{disk}/M_{tot}, where $M_{tot} = M_{disk} + M_{halo}$. The rotation curve of the exponential disk has its maximum at approximately $2R_e$ (see Binney
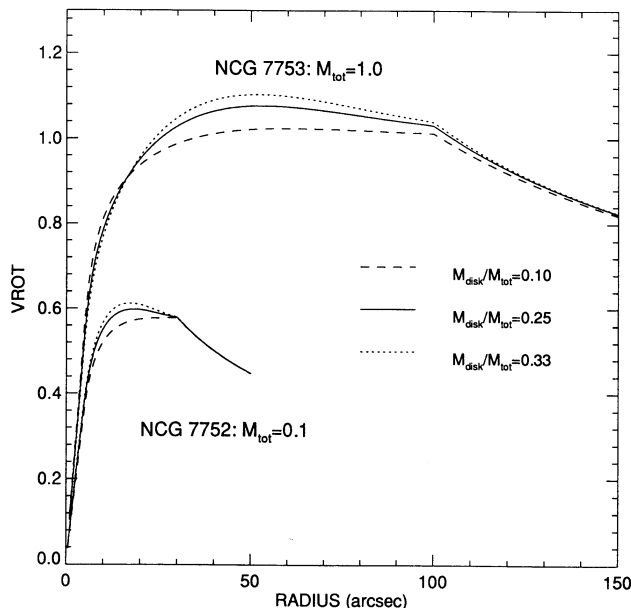

FIG. 1.—Adopted initial rotation curve models for NGC 7753 and NGC 7752, obtained by superpositions of truncated exponential disks and isothermal halos (see eqs. [4] and [5]). Depending on the ratio of disk to total mass, M_{disk}/M_{tot}, slightly different model rotation curves are obtained. Notice that in the simulations with finite velocity dispersion ($Q_T > 0$), the assigned mean tangential velocity is smaller than the circular velocity, owing to pressure support of random velocities. The correction factor is calculated with standard procedures (see Ostriker & Peebles 1973).

& Tremaine 1987). As the halo contribution is added, curves remain essentially flat to R_H. For most of our runs we concentrate on $M_{disk}/M_{tot} = 0.25$, which is estimated by the relation $M_{disk}/M_{halo} \propto L_B^{2/3}$ following Persic & Salucci (1990). It is worth noticing that the derivation of the dark matter fraction strongly depends on the adopted population synthesis model, and, for example, Jablonka & Arimoto (1992) did not find any evidence for significant enhancement of dark matter toward later type spirals.

According to the observations of Marcelin et al. (1987), the rotation curve of NGC 7753 attains a maximum at about 40'', after which the velocities drop about 30%, and 60% as 100'' is approached, in the eastern and western sides, respectively. The linear central portion has an extent of about 10''. As will be shown in § 4.6, the drop of observed velocities can be accounted by the interaction, and therefore we assume that the initial circular velocity curve is essentially flat also for $R > 50''$. By assuming that $M_{disk}/M_{tot} \approx 0.25$, the choice of $R_c = 0.25R_e = 5''$ gives a reasonable initial model. Somewhat arbitrarily, we set $R_H = R_d = 100''$ for most of the runs. For NGC 7752 the rotation curve has a linear portion of about 10'' and remains flat (east) or even slightly rising (west) to the last points measured by Marcelin et al., at $R = 20''$, which rising might be related to the interaction. Nevertheless, Persic & Salucci (1990) found that in general smaller galaxies have relatively less concentrated halos as compared with their disks, so that in the initial model for the secondary we assume $R_c = 1.25R_e = 5''$ and $R_H = 1.5R_d = 30''$. Figure 1 also shows the model rotation curves for the companion, based on a mass ratio of 0.1, which was estimated in Paper I from maximum rotation velocities.

3.1.3. Orbital Constraints

In the simulations scaled units are used. They are determined by setting the total mass of the primary M_1, its disk truncation radius R_d, and the circular velocity at R_d to unity. Therefore, 1 mass unit = $3.6 \times 10^{11} M_\odot$ (see Paper I), 1 length unit = $100'' = 25$ kpc, and 1 velocity unit = 250 km s^{-1}. With this choice the angular velocity at the disk edge is also unity, and one revolution at the edge takes 2π time units, each time unit (equal to the crossing time) thus corresponding to 25 kpc/250 km s$^{-1} \approx 10^8$ yr. From the CCD images, the separation between the components is about 110'', or 1.1 simulation units, at position angle 225°. The observed radial velocity difference, 220 km s^{-1} (Marcelin et al. 1987) corresponds to 0.9 simulation units (positive, since the companion is moving toward us relative to the main disk).

3.2. Survey of Orbits Matching the Orbital Constraints

The location of the companion at the end of the apparent bridge arm led Marcelin et al. (1987) to suggest that a direct encounter between the systems is just beginning. However, the outer tidal arms reach deep into the main disk in a continuous manner, which suggests that the disk of NGC 7753 has been exposed to the perturbation for quite a long time span. Also, the inner spirals are probably not directly excited tidal material arms but most likely density waves (see § 3.5) excited by the perturbations of the outer disk, also supporting longer duration for the passage. The overall regular structure also suggests that the perturbation is rather mild and old.

3.2.1. Preliminary Parabolic Experiments

In order to get a crude estimate of the possible type of interaction for the Arp 86 system, several preliminary experiments

were carried out by studying direct parabolic encounters with $R_{min} \approx 1 - 2R_d$, and point-mass companions with $m_{pert} < 0.2$. We concentrated on following the time evolution of the primary disk resulting from the essentially impulsive perturbation near the closest passage, thus not yet paying any attention to matching the observed separations. These experiments indicate that at $T = 1–2$ after the closest passage at $R_{min} < 1.5$, the outer parts show well-developed tail and bridge structures, which could be expected to match the Arp 86 system if viewed from an appropriate direction. However, at that time there is not yet any sign of the inner spiral structure, and only after $T = 3–4$ does the inner disk show any resemblance to NGC 7753. As compared with the location of the closest passage, the original bridge arm has then turned by almost 180° and is already dispersing.

3.2.2. Experiments with Accurate Orbital Search Method

Since the actual passage is not necessarily parabolic, the above conclusions concerning interaction age must be verified by studying the morphology in runs where observational con-

straints are fully taken into account. The orbital search method described in § 2.2 was then utilized, and various values of AZI for the most recent passage were studied. As the line defined by the projected position of the companion crosses the disk plane of NGC 7753 at AZI $\approx$ 170°, direct encounters correspond to upward crossing of the disk plane at some AZI < 170°, with smaller AZI requiring longer and longer duration since disk crossing. Three main types of orbits were found, all of which can pass through the present projected position at approximately the right radial velocity and, moreover, reproduce the outer tidal structures. Examples of various orbits and corresponding N-body experiments are displayed in Figure 2. Typically, crossing distances in the range $R_{cross} \approx 1.2–1.6$ were studied, but the results are not sensitive to its exact value.

Type I: near-parabolic encounters.—The first type of orbit is obtained by assuming that the upward crossing has occurred within about 100° from the present projected position, with AZI in the range 110°–70° (Fig. 2a, *thick solid lines*). The time matching the bridge location is determined empirically. For AZI in the above range, $T_{obs} = 1.3–2.0$ puts the bridge arm in
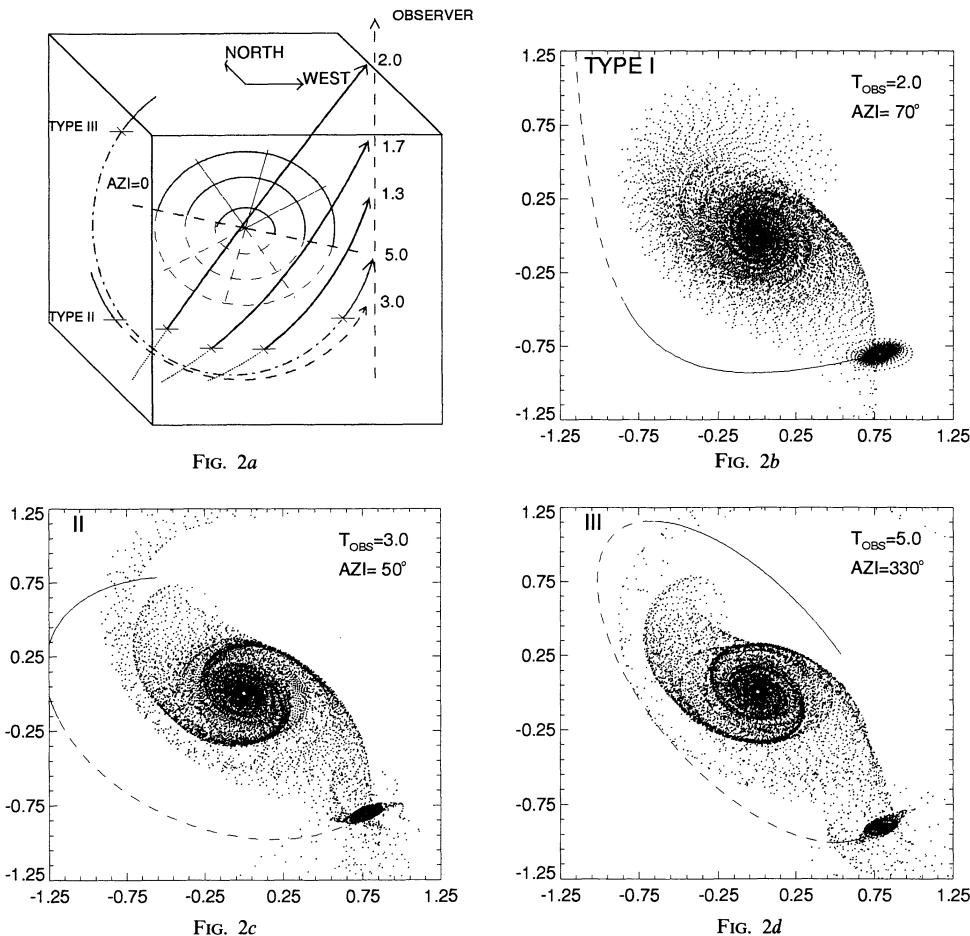

FIG. 2a

FIG. 2b

FIG. 2c

FIG. 2d

FIG. 2.—(a) Examples of various types of orbits matching the observational constraints and giving the right bridge location. The cube defines a sky coordinate system with the observing direction along the positive z-axis. The grid shows schematically the orientation of the disk of NGC 7753 (solid lines indicate the side closer to the observer). Azimuths are counted counterclockwise along the disk plane, from the line of the intersection between the disk and the sky planes (marked by AZI = 0). Companion orbits are shown by lines, solid above the plane of the main disk. Other frames give examples of the N-body experiments for each orbital type, and the projection of the system to the sky is shown, together with the relative orbit (dashed lines indicate the portion below the NGC 7753 plane). Standard initial disk models and 0.1 perturber mass are assumed. (b) Example of hyperbolic passage (type I). (c, d) Examples of low-inclination bound orbits, leading to companion location either slightly below (type II) or above (type III) the disk plane. The last type of experiment leads to the best observational match. Notice that in these experiments the companion self-gravity is ignored as in all the subsequent runs unless otherwise indicated.

the right apparent position. The relative orbit for AZI = 110°
is highly eccentric ($\epsilon \approx 0.7$) and transforms to hyperbolic as the
crossing is pushed farther away ($\epsilon \approx 1.5$ for AZI = 70°). At the
same time, the actual position of the companion is located
farther and farther above the plane of the main disk, because of
both longer elapsed time and increased inclination of the orbit
(for example, if AZI = 70°, $i_{orb} = 64°$ and the location of the
companion, z_{comp}, is 1.43 simulation units above the plane of
the main disk). For each of these orbits, the periapse is near the
disk-plane crossing. However, none of these encounters gives a
satisfactory model for the system: even in the simulation for
$T_{obs} = 2$ (Fig. 2b), there is yet no sign of the inner spiral struc-
ture, in agreement with the preliminary parabolic experiments.
Moreover, for these models the apparent location of the com-
panion at the end of the bridge arm would be a mere coinci-
dence.

 Type II: near-circular orbits without recent disk crossing.—If
the crossing azimuth is pushed farther away from the present
observed position, requiring longer time since crossing, no
near-parabolic or hyperbolic orbits of the above type were
found which would fulfill the observational constraints. The
problem seems to be that hyperbolic passage leading to the
right projected separation requires too high a radial velocity
difference. Instead, a second type of almost planar solution
appears for AZI = 50°–10° and $T_{obs} = 3$–4, involving a *down-
ward* crossing at the specified azimuth. For these orbits, the
companion is predicted to be moving toward the plane of
NGC 7753 but to be still slightly below it ($z_{comp} \approx -0.1$). As
can be seen from the experiment with AZI = 50°, $T_{obs} = 3$ (Fig.
2c), the obtained morphology bears a much better resemblance
to the actual system than in the previous example, although the
values of T_{obs} and AZI are not too different from those of
Figure 2b. This is due to the almost planar perturbation.
However, the fits are not totally satisfactory, since in all these
models the observed velocity difference is about 15% less than
actually observed.

 Type III: best-fitting near-circular solutions.—The most
promising models for the Arp 86 system are obtained by
assuming downward crossing in the range of AZI = 320°–360°
with $T_{obs} = 5$–6 (Fig. 2d; type III). For these models, the
implied orbits are almost circular, with $\epsilon \approx 0.05$–0.15, while
the inclination $i_{orb} \approx 20°$–30°. The morphology of the models is
rather similar to that of Figure 2c, but the orbital constraints
are more accurately fulfilled, within a few percent. Another
difference is the predicted present position of the companion:
in the models represented by Figure 2d the orbits have crossed
the disk plane of NGC 7753, and $z_{comp} \approx 0.20$–0.30. Notice
also that these orbits in fact follow from extending backward
the first type of orbits for AZI > 150°.

 In addition to morphological differences, the rotation curve
information also helps to distinguish between various possible
orbital geometries. Figure 3 displays the observed major-axis
rotation curve (adopted from Marcelin et al. 1987), together
with those derived from the simulations shown in Figure 2. In
the case of near-parabolic and highly inclined recent passage,
the simulated rotation curve is nearly unaffected by the pertur-
bation and retains its initial flat shape (Fig. 3b). On the other
hand, planar, longer-lasting perturbations lead to a clear drop
in the velocity curve (Figs. 3c and 3d), in accordance with
observations. An interesting difference between Figures 3c and
3d is the turning of the velocities in the vicinity of the compan-
ion, obtained in the latter model where the companion has
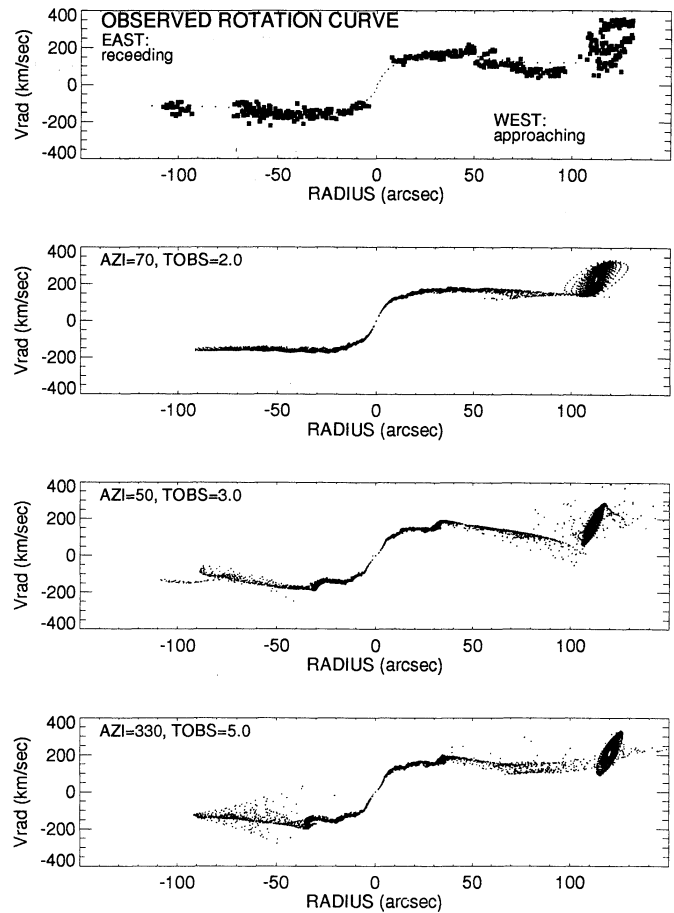passed the disk plane twice. The turn in velocity is caused by

FIG. 3.—Major-axis rotation curves corresponding to *N*-body experiments
of Fig. 2 are compared with that observed by Marcelin et al. (1987, Fig. 6).
Particles within 30° of the line of nodes are displayed. Notice that Marcelin et
al. correct their data to the plane of the NGC 7753 disk by assuming 52°
inclination: we have removed this scaling so that the points correspond
directly to observed radial velocities.

the companion perturbing the bridge it created about a half-
revolution before.

 Although the above described orbital survey is far from
complete, an important conclusion can be drawn: all satisfac-
tory models seem to require a rather circular, low-inclination
orbit. This implies that the companion has spent a long time in
the vicinity of the main system, which might have significant
long-term influence on the internal structure of both com-
ponents. We will later return to this question as well as address
the problem of how this type of orbital configuration might
have originated.

3.3. *Best-fitting Model*

 After the above-sketched extended orbital survey, another
series of simulations was performed, concentrating on relative
orbits with downward crossing at the azimuth range of 320°–
360° and $R_{cross} \approx 1.2$–1.6, and attaining the present projected
position at $T_{obs} \approx 5$–6. The simulations were started about 2–3
time units before the downward crossing and continued to the
present time. Therefore, in these models only the most recent
"half-orbit" is considered, and most of the obtained features
are excited near the downward crossing. For this rather short

orbital patch, the method outlined in § 2.2 works quite efficiently, and the final positions in simulations match the orbital constraints fairly accurately, especially if the more accurate method involving iterative small particle number simulations is employed. In this subsection we will compare the observed with the simulated morphology.

Figure 4 (Plate 5) compares one of the best models obtained with the observed V-band image. The main perturbation was caused by a downward crossing of a 0.1 mass companion at AZI $= 340°$, about 5.7 time units before the present time ($T_{obs} = 5.7$). This crossing occurred at a distance $R_{cross} = 1.5$, while the most recent upward disk-plane passage occurred at $T = 5.2$, or just 0.5 time units before the present. This corresponds to roughly 50 Myr, so that the companion is still near the plane of the main disk. It is also very close to the pericenter, which would occur at $T = 6.1$, $R_{min} = 1.15$. In this experiment, both the projected separation and the velocity difference match the observed ones within 5%. The model also matches most of the morphological characteristics of NGC 7753, both for the inner and the outer structure, as can be seen from the superposed symbols tracing the location of the observed spiral arms.

Taking into account the good fit for the morphology, it is not surprising that the overall features of the velocity field are also well represented. In Figure 5 (Plate 5) the above model is compared with the observed velocity field (drawn from data given in Fig. 3 of Marcelin et al. 1987). For example, the zero-velocity line curves along the bridge arm in a manner very similar to that observed. Also, the velocity kinks at inner density wave arms are visible.

In conclusion, it appears that the above "half-orbit" encounter model offers a good starting point for more detailed experiments where the dissipative gaseous component is included, as well as for studies of how the morphology is affected by successive orbital revolutions. However, before this, it is interesting to study how strongly constrained the obtained orbit is, by varying each of the important orbital parameters.

3.4. Effect of Model Parameters

The above model involves a large number of free variables, some of which are directly related to the relative orbit between the components and some to the assumptions made concerning the initial models. In order to estimate how well various parameters are constrained, a series of experiments was made by varying each of the important factors around the standard values of the above-described best model. Parameters related to the relative orbit (AZI, T_{obs}, R_{cross}) as well as to the initial model assumptions (M_{pert}, softening length ϵ_{soft}, and M_{disk}/M_{tot}, i_{disk}) were tested.

Many of these factors have similar influence on the obtained features and can thus hardly be separated with great accuracy. For example, increased R_{cross} leads to weaker inner spiral structure, but it can be somewhat compensated for by increasing the perturber mass or by allowing a longer time since the passage, which, however, cannot be altered too much from $T = 5$–6 in order to maintain the bridge location. On the other hand, too strong perturbation tends to reduce the size of the inner spirals and cause unacceptably strong deformations at the outer regions. Therefore, for M_{pert} between 0.05 and 0.15, R_{cross} in the range 1.3–1.6 seems to be required. Also, the difference between observed and simulated morphology increases rapidly if the azimuth of downward crossing is varied, say, more than 20° from AZI $= 340°$. The good match of the standard model is also due to the use of the correct scale length based on observations, since deviations from the true scale length affect the form and scale of the excited inner density waves.

The value assigned to M_{disk}/M_{tot} affects the growth rate and amplitude of inner density waves (Fig. 6). For example, for the ratio of 0.1 the inner spirals do not extend very deep and simultaneously appear to have too wide an opening angle. On the other hand, M_{disk}/M_{tot} could be increased to 0.33 and the main features remain essentially the same, except stronger and somewhat kinkier. If disk mass is further increased, the disk becomes susceptible to bar instabilities, in accordance with several previous simulation studies (e.g., Sellwood 1985; Salo 1991). In connection with varying the relative contribution of a self-gravitating disk, the sensitivity of the results to the softening length was also examined, by studying values of ϵ_{soft} in the range 0.03–0.07. Although reduced softening mimics the effects of increased disk mass ($\epsilon_{soft} = 0.03$, $M_{disk}/M_{tot} = 0.25$ is very similar to the case $\epsilon_{soft} = 0.05$, $M_{disk}/M_{tot} = 0.33$), the main morphological features remain the same.

In Figure 6 the sensitivity to the assumed viewing direction is also studied, by varying the inclination of the primary disk. Because the estimated maximum rotational velocity depends on i_{disk}, in each case the observed velocity difference converts to a slightly different value in the simulation units, $v_{obs} \approx 0.7$, 0.9, 1.1 for $i_{disk} = 30°, 40°, 52°$, respectively. Whereas the difference between $i_{disk} = 30°$ and 40° is small, for $i_{disk} = 52°$ it is not possible to avoid getting an inner spiral structure that is too elongated. This is easy to understand in light of Figure 4 of Paper I, where the inclination-corrected image appears clearly overcorrected for $i_{disk} = 50°$. This gives further support for our use of a revised disk inclination as compared with the value adopted by Marcelin et al. (1987).

Some experiments were also carried out increasing the halo truncation radius R_H from its standard value of $5R_e$. This affects the orbital speed of the companion and therefore changes slightly the times required for reaching the present position for a given AZI. However, the effects on the morphological features of the main disk are too small to set any constraints on R_H. On the other hand, the initial estimate for the disk truncation radius ($R_d = 5R_e$) seems to be slightly too large, since the particles near the outer edge are responsible for the narrow extended tail structure seen, for example, in Figures 2c and 2d. For example, in Figure 6 the particles initially outside $4.5R_e$ have been excluded from the plots, thus suppressing this feature. However, we will show in § 3.6 that the outer portions of the main disk are in any case strongly affected by the long-term perturbation history, so that the initial choice of the stellar disk truncation radius is quite irrelevant.

3.5. Gas Component and Star Formation

In the previous experiments only the stellar component of the main disk was studied, although the cool component with initial $Q_T = 0$ mimics to some extent the short-term behavior of gas. In this section we include the dissipative gas component and also study the preferred locations of star-forming regions in terms of OB particles.

Figure 7a displays the time evolution in a simulation including colliding gas particles in the main disk. The gaseous component was modeled by an exponential disk but had 1.5 times larger R_d (1.5) and R_e (0.3) as compared with the stellar disk. This accounts in a qualitative manner for the typically increasing relative contribution of gas in the outer parts of the galactic
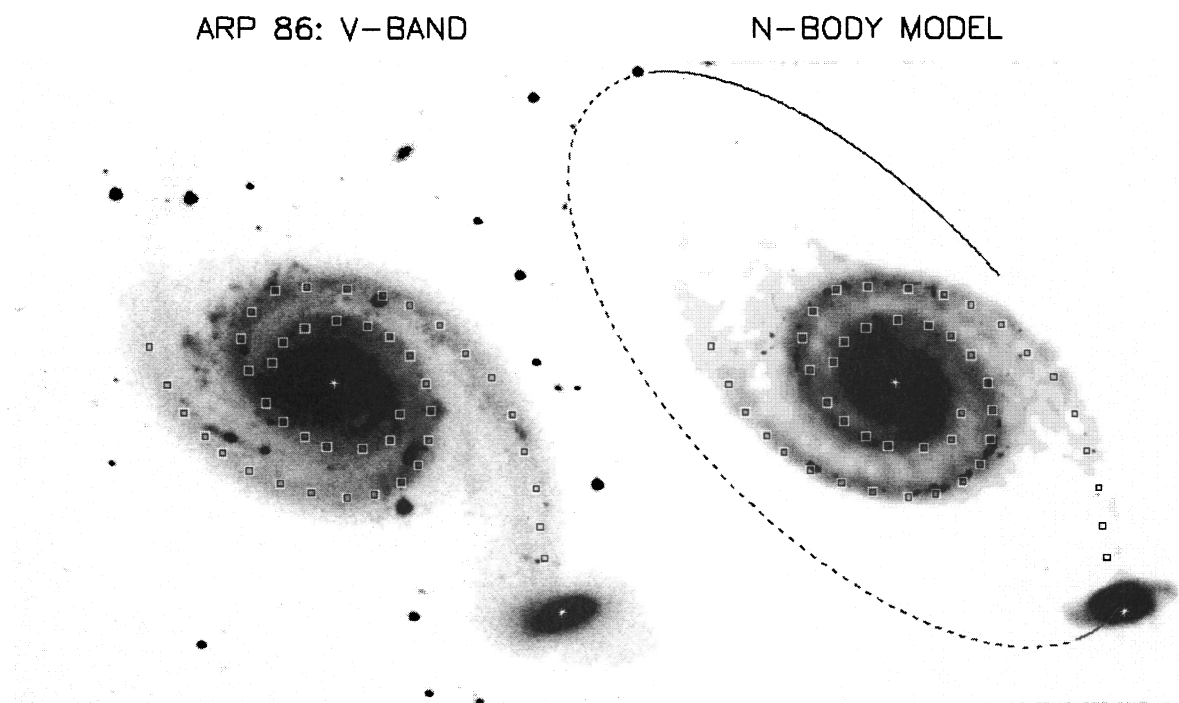
ARP 86: V-BAND   N-BODY MODEL

FIG. 4.—Comparison of the observed V-band morphology and the best "half-orbit" simulation model, shown at the same scale. The disk component was described with the standard parameter values ($R_{disk} = 1.0$, $R_e = 0.20$) and consisted of 30,000 "warm" particles with Toomre parameter $Q_T = 1$ and 10,000 cold particles with $Q_T = 0$. The softening length was set to $\epsilon = 0.05$, and a $36 \times 36 \times 19$ grid was employed, covering the radial extent from 0.01 to 5.5 simulation units. The companion consisted of 7500 warm and 2500 cold particles. Integration step size was 0.01, corresponding to ≈ 60 steps per orbit in the inner parts of the main disk and 630 steps per orbit near the truncation radius. Orbital parameters of the simulation run are described in the text. The dashed line indicates the portion of the orbit below the plane of the main disk. The simulation plot is obtained by transforming the stellar particle distribution to a density table with 0.02 bin size. Also shown are the locations of highest OB particle densities in a simulation of Fig. 7.
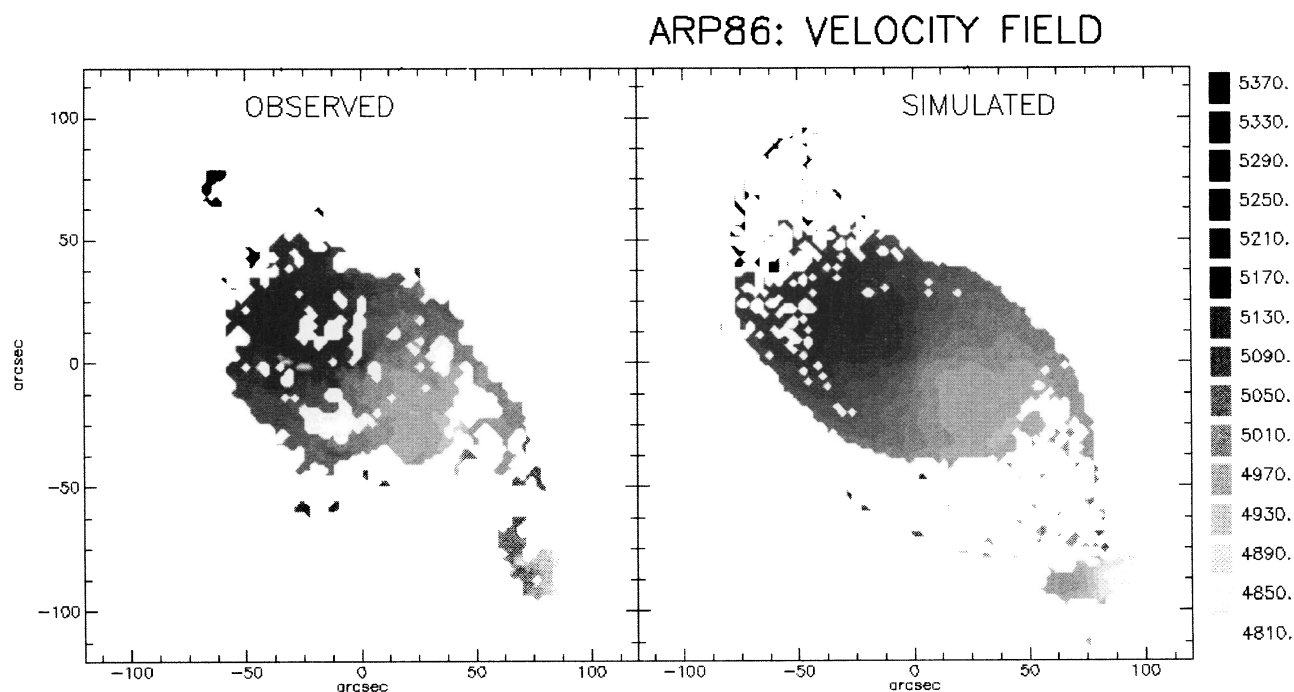
ARP86: VELOCITY FIELD

FIG. 5.—Observed velocity field (data taken from Marcelin et al. 1987, Fig. 3) compared with that of the simulation of Fig. 4
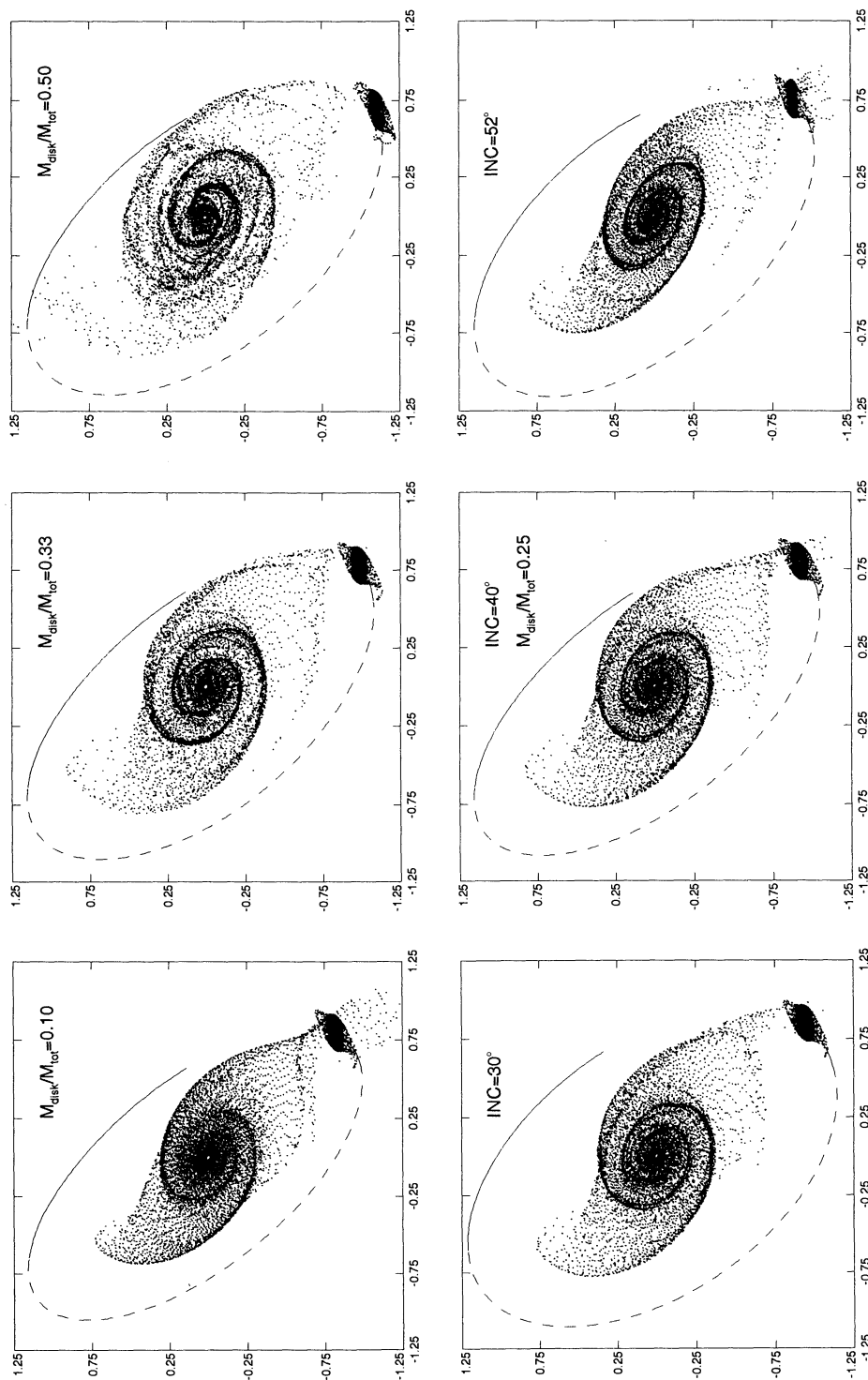
FIG. 6.—*Top panels:* Effects of changing the relative contribution of the disk mass: $M_{disk}/M_{tot} = 0.10$, 0.33, and 0.50. *Bottom panels:* The inclination assigned to NGC 7753 disk is varied: $i = 30°$, $40°$, and $52°$ ($M_{disk}/M_{tot} = 0.25$). Notice that changing the inclination changes the derived rotation amplitude and thus the scaled relative speed between the components: for $i = 30°$, $v_{obs} = 0.7$, while for $i = 52°$, $v_{obs} = 1.1$; the different projection angle is also taken into account.

594
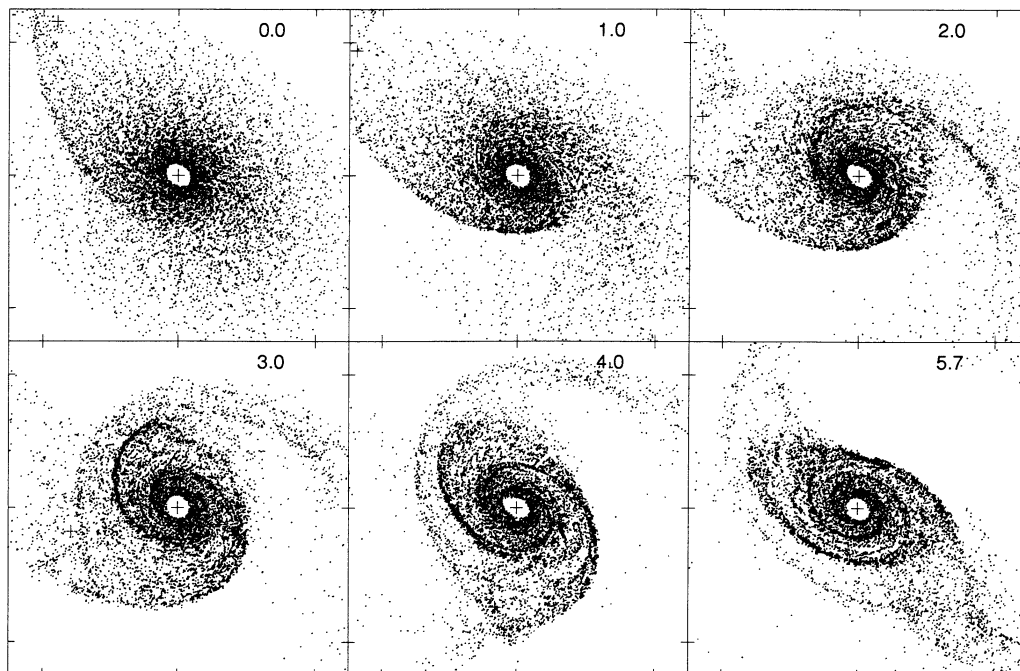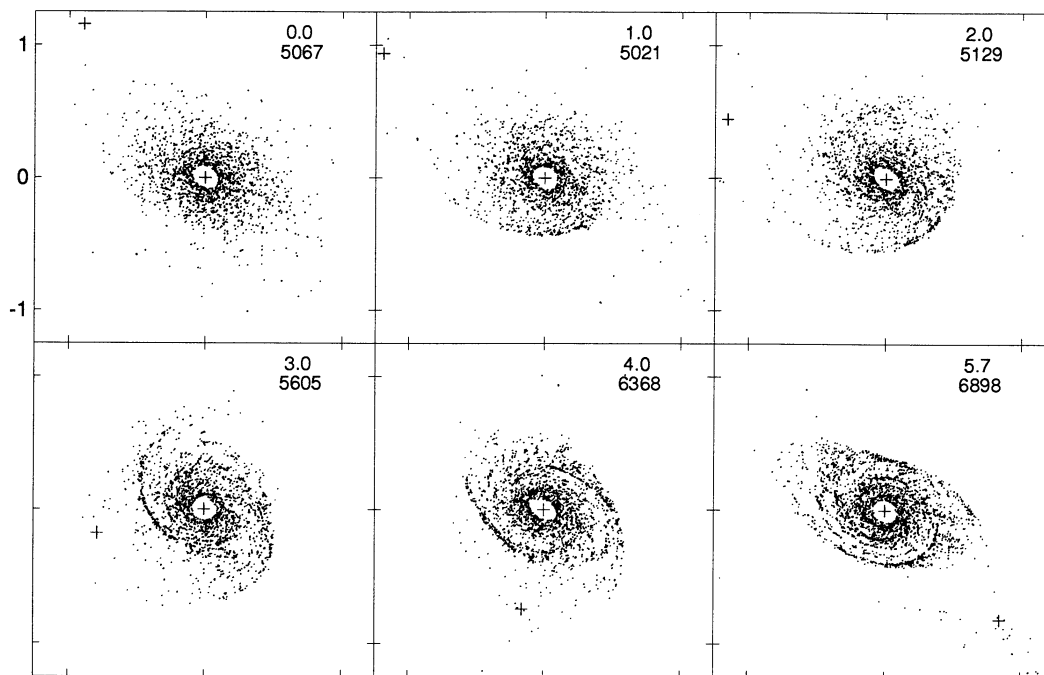
FIG. 7a

FIG. 7b

FIG. 7.—(a) Time sequence of the gas distribution in a simulation with the same orbital parameters as the best-fitting model. A total of $N_{gas} = 10,000$ massless colliding particles (with $\sigma = 0.0025$, $\alpha = 0.0$, $\beta = 1$) were distributed in an exponential disk with $R_{disk} = 1.5$, $R_e = 0.30$, in addition to a self-gravitating stellar disk of 30,000 particles with $R_{disk} = 1.0$, $R_e = 0.20$. The companion was treated as a point mass. Projection to the sky is shown at various times, with the companion marked by a cross. (b) OB particles (with age < 2 time units) are shown for the same run. The last frame, transformed to a density plot, was included in the simulated image of Fig. 4.

595

disks and, moreover, helps to emphasize the weaker outer features. Also, in order to speed collisional calculations, the innermost region $R < 0.1$ was left unpopulated. Since no mass was assigned to gas particles, the rotation curve was unaffected. Rather extreme collisional parameter values were adopted: in each impact the relative velocity between particles was reduced to zero, $\alpha = 0$, $\beta = 1$, thus mimicking the gravitational growth processes stimulated by material compression. However, after impacts the particles were allowed to separate, so that no attempt was made to model the actual growth of cloud complexes.

According to Figure 7a, showing the distribution of gas at various times, several phases in the evolution can be distinguished. Initially, the gas compression is strongest at the bridge arm forming around the downward crossing at $T = 0$, but quite soon the compression in tail regions starts to dominate ($T = 2$–3). This behavior is a rather generic feature, and takes place for a large range of orbital parameter values, as also demonstrated by the parabolic test particle experiments of Wallin (1990). However, in our model involving a closed orbit, the companion catches the bridge arm again, and induces a second compression phase near the upward crossing, $T = 5$–6. Without the second passage, at the corresponding time the bridge arm would already have almost dispersed. The above sequence is also visible in the plots of young OB particles (Fig. 7b). In addition to compression of the outer regions, density waves excited in the inner stellar distribution lead to strong gas compression. The overall increase in the formation rate of OB particles in the main disk is about 40%, as compared with the level in the absence of perturbation. This increase starts about 2 time units after the initial crossing, or when the tidal bridges and tails start to form. It is interesting to notice that, at least in this experiment, the strongest OB particle formation region outside the nuclear regions, in the southwest direction, corresponds quite closely to the strongest observed star-forming regions (marked in Fig. 4; see also Paper I, Fig. 1).

Figure 8 displays in more detail the distribution of OB particles at the time corresponding to our present observing instant, $T = 5.7$, in a run similar to that in Figure 7, except for slightly higher impact frequency. The most notable feature, along the concentration to spiral arms, is the spurlike condensations emerging outward from the inner spirals, which trailing elongated structures are most prominent near the southwest and northeast directions. These features are related to density waves in simulations. The movement of individual particles with respect to spiral arms is shown in Figure 9: at the tidal arms, gas particles comove with the outer arms (material waves), whereas the inner arms exhibit clear density-wave character, particles catching and leaving the compression regions. The density-wave character is probably the explanation of why the spurs are seen only in the inner regions: gas clouds collide predominantly in the compression regions, which tends to synchronize their movement also when they have left the wave. On the other hand, gas clouds in the material arm cannot leave it. The formation of these spurs depends somewhat on the collisional parameters, but they are still visible even if $\alpha = 0.25$, $\beta = 0$, which corresponds to much less dissipative impacts.

This kind of spurlike structure is visible also in the CCD images (see Fig. 1 of Paper I). The fact that the spiral arms are divided into material and density waves probably affects the way stars are induced there, as noted in Paper I. According to observations, the inner tidal bridge shows signs of stellar for-
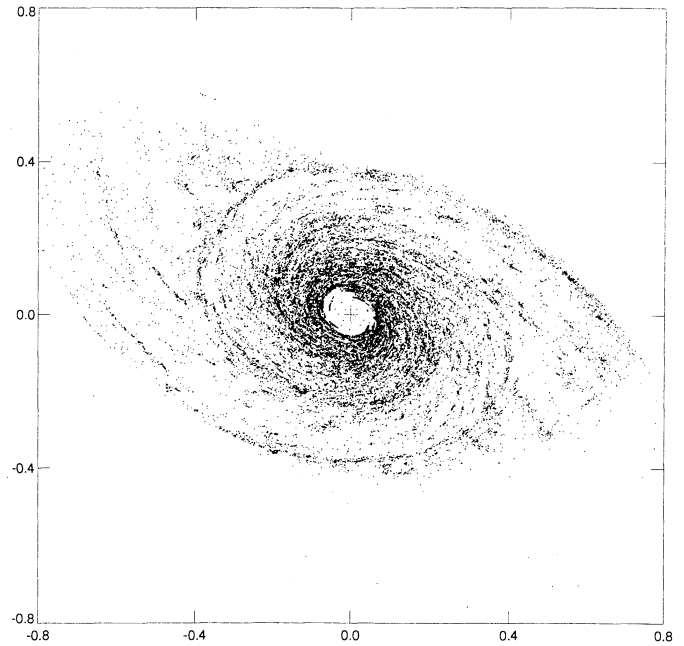

FIG. 8.—Distribution of young OB particles (with age <2) in an experiment similar to Fig. 7, except with a slightly larger impact frequency ($\sigma = 0.005$, $N_{\mathrm{gas}} = 5000$). Projection to the sky at $T = 5.7$ is shown, corresponding to the present time.

mation, which is concentrated to the concave edge of the arm. Although the simulated OB distribution lacks the necessary resolution, some signs of this type of phenomena might be visible for example in Figure 6 with $M_{\mathrm{disk}}/M_{\mathrm{tot}} = 0.33, 0.25$. In the density-wave portion of the tail there is an outward bump near the southwest direction (see last frame of Figure 9 at $\phi = 30°$), which might be due to the companion perturbing the density-wave region.

According to Paper I, the tip of the bridge arm is very blue, with $B - V \approx 0.2$–0.4, most probably indicating recent enhanced star formation. Also, several strong star-forming complexes are present there, more than in the intermediate regions of the bridge. An interesting possibility is that the star formation in the tip is enhanced due to local gravitational instabilities leading to growth of large cloud complexes, even if the overall density is low. According to Kennicutt (1989), star formation is possible in regions where the local gas surface density Σ_{gas} exceeds a threshold density Σ_{cr}, related to the simple Toomre stability criterion for the gas component:

$$\Sigma_{\mathrm{cr}} = f \frac{\kappa c}{3.36G}, \qquad (6)$$

where c is the gas velocity dispersion and f is a dimensionless constant near unity. According to Kennicutt (1989), once $\Sigma_{\mathrm{gas}} \approx \Sigma_{\mathrm{cr}}$, the star formation rate (SFR) increases nonlinearly as a function of Σ_{gas}, whereas for $\Sigma_{\mathrm{gas}} > \Sigma_{\mathrm{cr}}$ it follows a typical Schmidt law with $\mathrm{SFR} \propto (\Sigma_{\mathrm{gas}})^N$, where $N \approx 1.3$. If c is assumed to be constant throughout the galaxy, Σ_{cr} is approximately inversely proportional to distance in the galaxy with a flat rotation curve ($\kappa \propto R^{-1}$). Combined with an exponential drop in Σ_{gas}, this implies a certain radius outside which star formation is suppressed. However, during the interaction, bridge and tail arms show considerable density enhancements, so that the onset of gravitational instability might be enabled
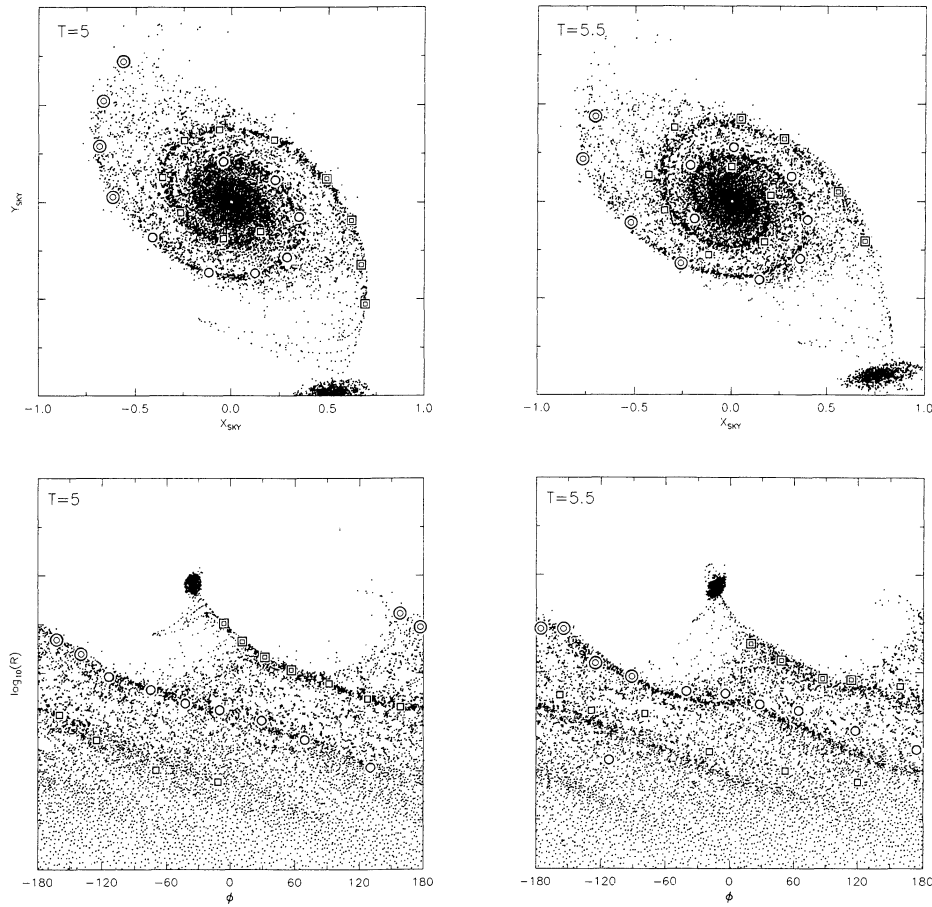
FIG. 9.—Density-wave and material wave regions. In the upper frames the distribution of the cool component in the run of Fig. 4 is displayed at two instants ($T = 5$ and $T = 5.5$), projected to our viewing direction. Symbols stand for selected particles tracing the tail (*circles*) and the bridge (*squares*) features at $T = 5$, and the location of the same particles is also shown for $T = 5.5$. Lower frames show the same particle distributions in (ϕ, log R) coordinates, in the simulation coordinate system aligned with the plane of the primary disk. Angle is counted counterclockwise from the major axis at P.A. $= -127°$. Double symbols mark particles that stay at the compression regions, indicating material-arm–like movement, in contrast to other locations where particles move faster than the density-wave condensation regions.

also at larger distances, especially where κ is small. As our simulation model based on potential grids does not include any direct cloud-cloud gravitational forces, small-scale insta- bilities cannot be followed. Therefore, we will use the simulated gas densities together with Kennicutt's criterion to address the possibility of gravitational instability and enhanced star for- mation in the tidal arms.

In Figure 10*a* we have applied Kennicutt's (1989) criterion for our initial gas distribution. The radial dependence of Σ_{gas} and Σ_{cr} is shown, based on the H I gas mass estimate of $1.6 \times 10^{10} M_\odot$ (see Paper I) (the total gas mass is not known) and a hypothetical exponential model with scale length 0.3, and the adopted rotation curve. Constant velocity dispersion $c = 6$ km s^{-1} is assumed, and $f = 1$. According to Figure 10*a*, these parameter values restrict initial star formation to $R < 20$ kpc or 0.8 simulation units. Notice that physical units are used only for illustrative purposes, as they do not correspond to any measured gas distribution: the exact numerical values are therefore not significant, only indicating relative trends. The surface densities along the bridge and the tail compression regions for the simulation of Figure 7 at time $T = 5$ are shown in the next frame, for regions marked in Figure 10*b*. As can be seen, the estimated Σ_{gas}/Σ_{cr} in fact increases along the bridge,

thus offering a possible explanation for observed star forma- tion at its far end. For the tail Σ_{gas} drops faster than Σ_{cr} as the distance is increased, in accordance with the lack of strong recent star formation. However, these results are only qualitat- ive, because of arbitrary gas density distribution and because it is rather uncertain whether the simple global collapse criterion holds for local, externally perturbed regions. For example, the original $\kappa(R)$ relation has been assumed, and the possible rise of gas random velocity has been ignored.

Although this model has its limitations, it offers a better explanation for the blue color of the bridge than, for example, the relative decrease of the old stellar population toward the outer regions of the galaxy, combined with differential reddening. Tidal stripping is not a good explanation either, because the two spiral arms have different colors, and accord- ing to our simulations the bridge and the tail material originate in the same initial radial zones of the galaxy disk. Simulations also predict that collision of the two gas disks (if we assume a very extended disk for the companion) tends to destroy the bridge near the satellite rather than to induce local gravita- tional collapse followed by star formation. As noted in Paper I, the color difference between the tail and the bridge is even stronger in $V - R$ than in $B - V$. This is in agreement with the
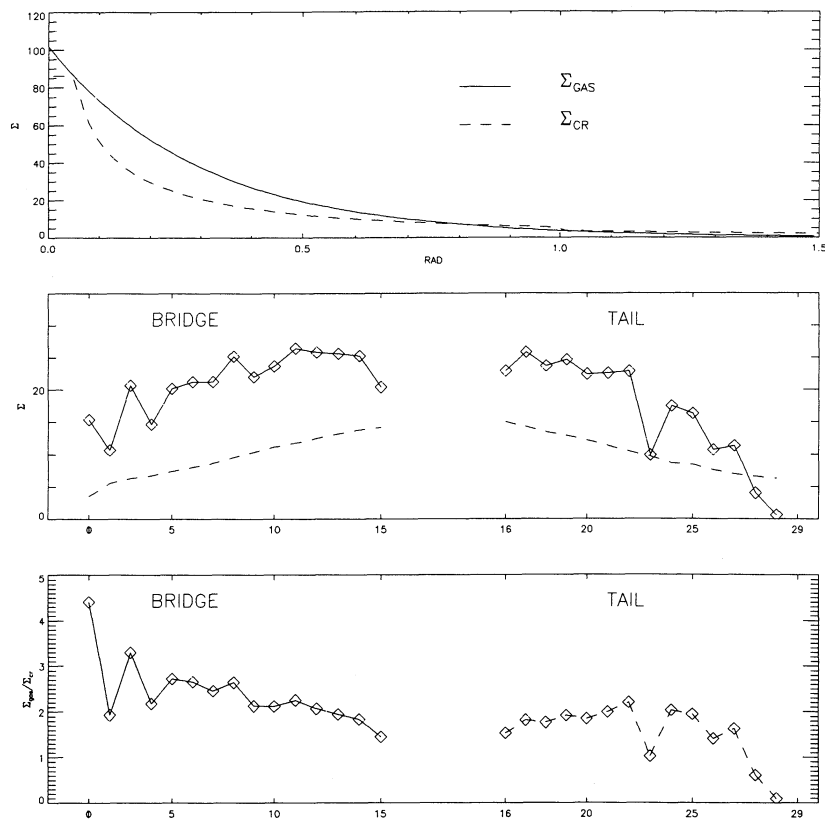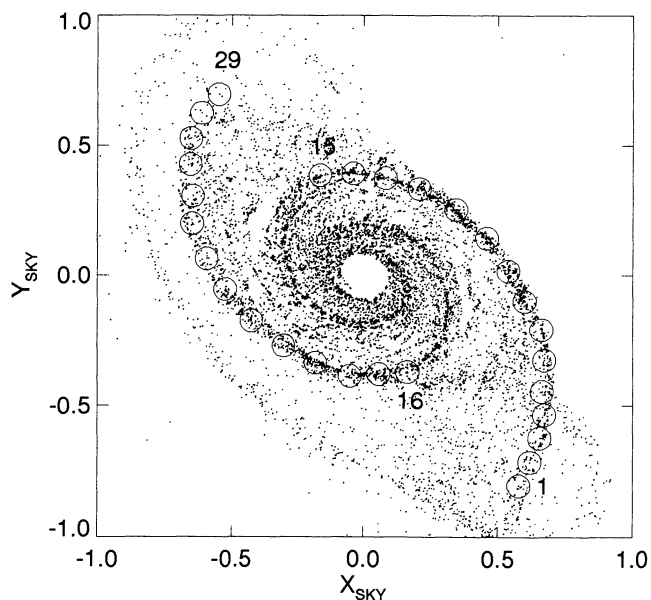
FIG. 10a

FIG. 10b

FIG. 10.—(a) Top panel displays the original gas surface density Σ_{gas}, together with the critical gas density Σ_{cr} corresponding to $Q_T = 1$ in the case of constant 6 km s^{-1} velocity dispersion. The middle panel shows Σ_{gas} and Σ_{cr} along the bridge and tail arms, in the run of Fig. 7 at time $T = 5.0$. The bottom panel compares the ratio Σ_{gas}/Σ_{cr} along the bridge and tail. Physical units ($M_\odot$ pc^{-2}) are used, although the exact numerical values are not significant owing to the use of hypothetical initial distribution. (b) Locations of the measurements areas used in (a) are displayed. Notice that measurements were made in the disk plane, whereas this plot shows the projection to the sky.

multiple-encounter history deduced for Arp 86, indicating that the companion must have disturbed the bridge for a long time, possibly during the course of several revolutions. The red $V - R$ color near the companion is discussed in Paper I.

3.6. Long-Term Evolution

As the best-fitting model for the most recent half-orbit implies an almost circular orbit, $R_{max} \approx 1.5$, $R_{min} \approx 1.15$, the strength of the tidal forces varies only weakly with respect to time. Therefore, the chosen starting point of our simulation model is quite arbitrary, and some of the obtained morphological features might be significantly altered by including the previous interaction history. The rather unexpected orbital configuration itself is most probably explained by the dynamical friction that has almost circularized the initially more elongated, perhaps only marginally bound relative orbit. Therefore, Arp 86 could well represent an interesting intermediate evolutionary phase: although having experienced strong orbital braking, it is still rather far from merging. Since it is practically impossible to guess the initial orbital configuration, we will instead study the future orbital evolution implied by the best-fitting model. Since the dynamical friction gets progressively stronger as the orbit shrinks, any morphological changes during the future orbital revolutions will be much stronger than those due to previous interactions in a more extended relative orbit. Therefore, the changes during the next revolution set upper bound for the possible remnants from previous passages.

Figure 11 displays a time sequence of simulation extending to $T = 30$, during which time the systems have completed
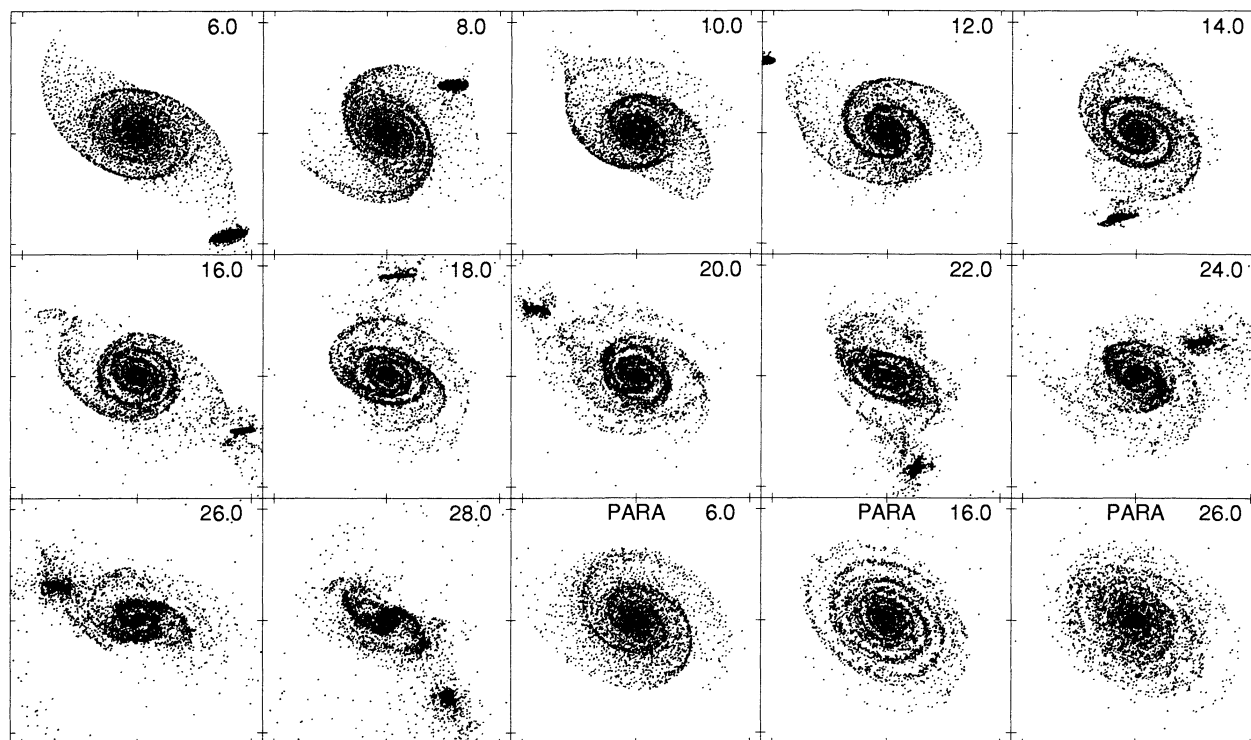
FIG. 11.—Long-term evolution in a run extending to $T = 30$, or over three complete revolutions past the present time. The systems consisted of $30,000 + 7500$ warm particles ($Q_T = 1$) and $10,000 + 2500$ cool particles ($Q_T = 0$); the distribution of the latter is displayed, projected to our viewing direction. Companion self-gravity was ignored. Initial downward crossing occurred at AZI $= 330°$, $R_{dist} = 1.6$. In the last three frames, selected times from a corresponding parabolic experiment with minimum distance $R_{min} = 1.5$ at AZI $= 330°$ and the same perturber mass 0.1 are shown for comparison. The size of each frame is 1.1 simulation units.

three full revolutions. Compared with the best-fitting half-orbit model (Fig. 4) R_{cross} was increased from 1.5 to 1.6, so that the initial perturbation is at least slightly weaker. At $T = 30$ the orbit has shrunk considerably (Fig. 12, *dashed lines*), and the systems are not far from merging. Because the simulation method does not allow halo deformations, only disks can convert energy of relative orbital motion to internal random motions, and the amount of dynamical friction is thus probably somewhat underestimated. Therefore, the actual merging process might in fact be even faster. Also, additional experiments showed that relatively small changes in the adopted present orbital parameters can decrease the final merging time scale significantly, although the orbital behavior during the next full orbit is hardly affected (see the solid lines in Fig. 12, corresponding to smaller starting distance).

Several important features can be noticed in Figure 11. First of all, the outlook of the system after the first two successive upward crossings ($T = 6.0$ and $T = 16.0$ correspond most closely to the present relative position) is not too different, implying that the features obtained in the above half-orbit fittings should not be too much altered by the previous, weaker interaction history. However, as the strength of the inner features increases with respect to time, a slightly larger present orbit might be allowed than is implied by the above best-fit "half-orbit," but this does not alter significantly any of our previous conclusions. Second, the gross features of the system are fairly similar at all times, with widely opening outer spiral arms pointing to the direction toward and opposite to the companion. This is in clear contrast to the time evolution in the parabolic encounters, where the spirals wind rapidly and the bridge soon loses any connection with the perturber. The

corresponding parabolic experiment in selected times is also shown in Figure 11. Indeed, this tendency of the bridge to follow the perturber might explain why so many M51 type grand-design galaxies are observed and why they all have such similar appearance: if they represent systems with low-eccentricity relative orbits, their outlook should indeed be only weakly dependent on the time we happen to observe them. Moreover, during successive close passages the open spiral structure seems to be periodically enhanced: see Figure 13, comparing the pitch angles of best-matching spiral fits at various times. A third interesting feature is the deformation of the tail at successive passages: while after the first passage the tail has a regular peaked appearance, after one complete revolution an irregular particle concentration appears at its end (see, e.g., $T = 16$ in Fig. 11). This kind of feature is also visible at low intensity levels in observed images (Fig. 3 in Paper I), thus giving further support to our multiple-encounter model.

We also checked how the velocity field behaves in the course of extended perturbation. As shown in Figure 3d, already, after the first half-orbit the initial, almost flat rotation curve is deformed to one with negative slope at $R > 50''$, in accordance with observations. During successive encounters this tendency becomes more pronounced. Also, the drop is more prominent on the western side, also in accordance with observations. This might also be related to the fact that the initial bridge arm tends to retain its identity at successive revolutions.

During the interaction, the outer regions of the primary component suffer from considerable tidal stripping. For example, practically all particles with initial radial distance exceeding $4R_e$ end up in the vicinity of the companion, or at
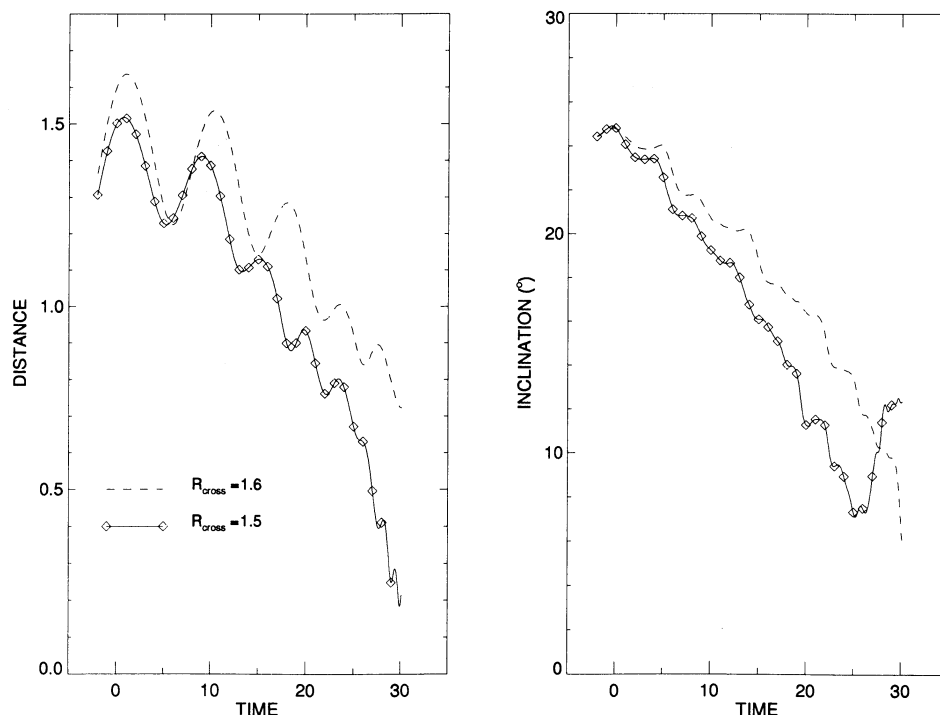
FIG. 12.—Time evolution of mutual separation and orbital inclination in the long-term run of Fig. 11 (*dashed lines*). Also shown is the orbit in a similar run, except with smaller initial separation $R_{dist} = 1.5$ instead of $R_{dist} = 1.6$ (*solid lines and diamond-shaped symbols*).
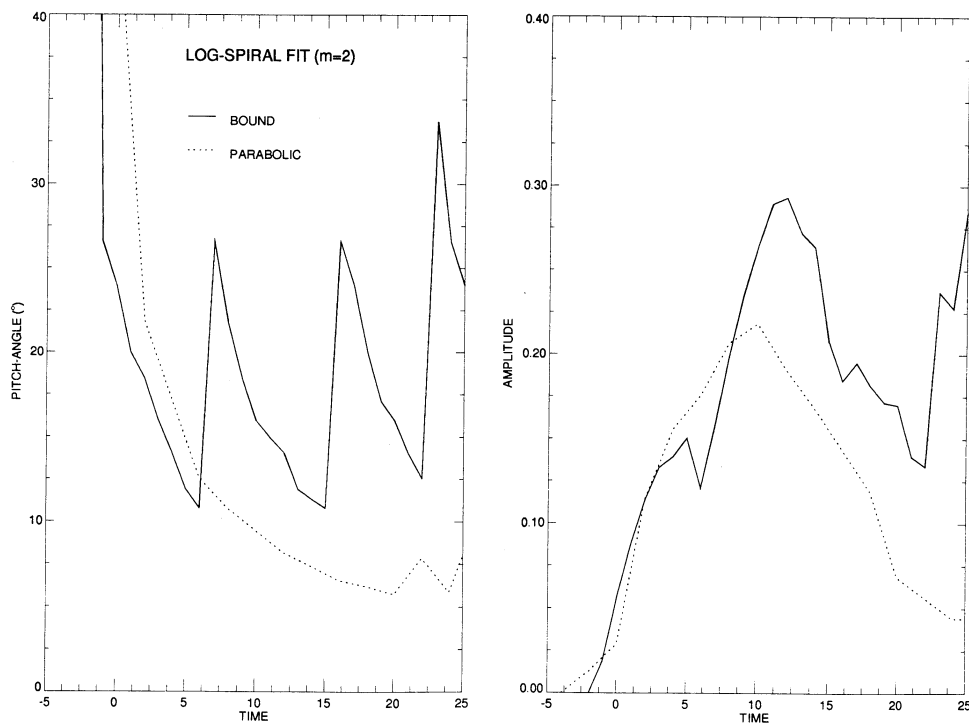

FIG. 13.—Evolution of the pitch angle of the tidally induced spirals in the long-term run of Fig. 11. The particle positions within $0.1 < R < 1.0$ were fitted by $m = 2$ logarithmic spirals of the form $\log R = -(m/p)(\phi - \phi_0)$ with various pitch angles, $\tan^{-1}(m/p)$. The pitch and amplitude of the best-fitting spiral are displayed (*solid lines*). For comparison, the evolution in the corresponding parabolic passage is also shown (*dashed lines*).
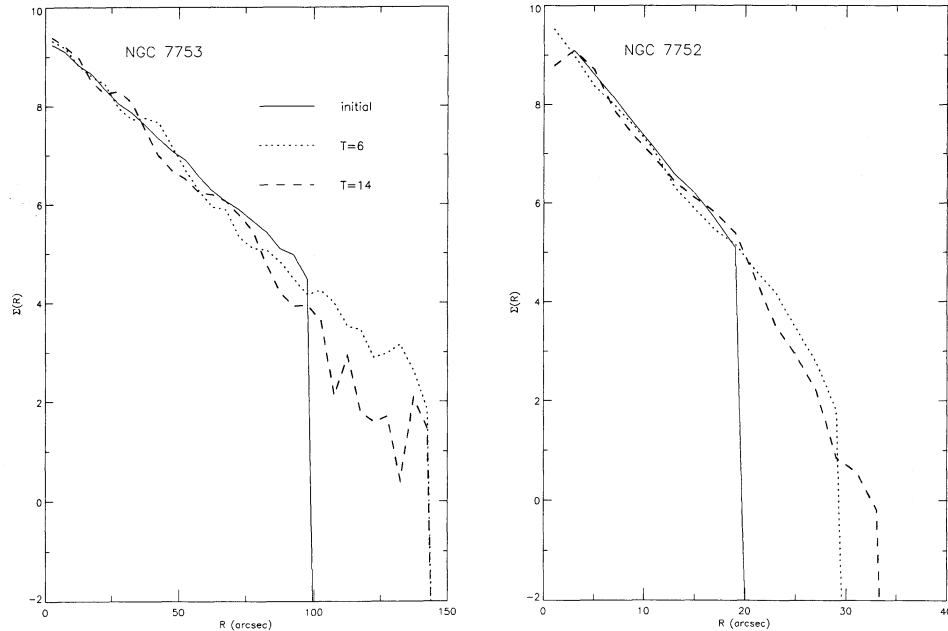
FIG. 14.—At left, the long-term evolution of the stellar distributions in the run of FIG. 11. Surface densities of initial truncated exponential model (*solid line*) are compared with those observed for $T = 6$ (*dotted line*), and one revolution later, $T = 14$ (*dashed line*). Also shown is the evolution of the companion disk in a run of Fig. 15a.

the narrow, rapidly dispersing outer tail structures. In Figure 14 the evolution of the stellar surface densities is displayed after successive passages. At later evolutionary stages the disk is seen to extend past the initial extent of 5 exponential scale lengths, but the density falls below the exponential model already for $R \approx 3R_e$–$4R_e$. In § 3.7, concentrating on the evolution of the companion, we will address the fate of the escaping material and estimate the amount being captured by the companion.

3.7. *Companion*

So far we have concentrated on the evolution of NGC 7753. However, the companion will also suffer severe tidal deformations. A crude estimate for the relative strength of the perturbation can be obtained by estimating the Dahari parameter for both systems (Dahari 1984). For approximately parabolic encounters $Q_D = (M_{pert}/M_{tot}) (R_{disk}/R_{min})^3$ gives a rough measure of the tidal damage expected from encounters with various relative masses and minimum separations. Using the separation distance of the downward crossing, $R = 1.5$, and disk sizes of 1.0 and 0.2 combined with the mass ratio 0.1, $Q_D = 0.03$ and 0.02 for the main system and the companion, respectively. Therefore, the perturbation experienced by NGC 7752 is at least of the same order as that of NGC 7753. However, if we instead use the minimum separation near the upward crossing, $R = 1.2$, and moreover assume that the initial extent of the companion is 0.3 (corresponding to the faint outer envelope; see Paper I), $Q_D = 0.06$ and 0.16. For the main disk, both estimates indicate relatively mild perturbation—for example, below the threshold $Q_D \approx 0.1$ required for tidal triggering of stellar bar formation in an otherwise stable disk + halo system resulting from direct parabolic passage (see Salo 1991: type I rotation curve). The larger estimate for the companion indicates that oval deformation of the stellar distribution might be sufficiently strong to lead to formation of a gas ring at the inner Linblad resonance. Note, however, that

the above estimates are strictly applicable only to the case of impulsive, direct encounter, and it is therefore unclear how they are modified in the case of continuous influence of the perturber at a low-eccentricity orbit, which should lead to stronger tidal effects. On the other hand, as seen from the companion, the relative orbit is highly inclined for either of the two possible orientations of its disk plane, which reduces the perturbation.

Because of the size difference, a factor of ~ 5 in the linear extent of the components of Arp 86, it is hard to study the internal structures with great accuracy simultaneously for both components. For example, our standard softening length, 0.05, is of the same order as the disk scale length of the companion. This poor resolution of the gravitational field might, for example, suppress the tendency for bar formation in the companion. Therefore, separate experiments for the companion were performed, where the main system was replaced by a halo potential model, and all the self-gravitating particles were in the companion disk and a 5 times smaller value $\epsilon_{soft} = 0.01$ was used. The time step was also reduced (from 0.01 to 0.005), to improve the overall accuracy of the integrations for the companion (this step size corresponds to about 250 steps per orbit in the interior and 600 in the outer parts) (see Fig. 1). The relative orbit between components was approximately same as in the best-fit model (slight changes follow from replacing the mass of the main disk component by adding it to the spherical component).

Figure 15 displays the time evolution of the companion in an experiment including self-gravitating stars and nongravitating, colliding gas, for the two possible orientations (Fig. 15a corresponds to the orientation with the northern side closer to the observer and $i_{rel} = 40°$ [*ori* = 1], while in Fig. 15b the southern side is closer and $i_{rel} = 83°$ [*ori* = 2]). In both cases the projection to the initial companion disk plane is shown. The first orientation corresponding to direct passage of the main system displays the typical tidal bridge and tail features, whereas for
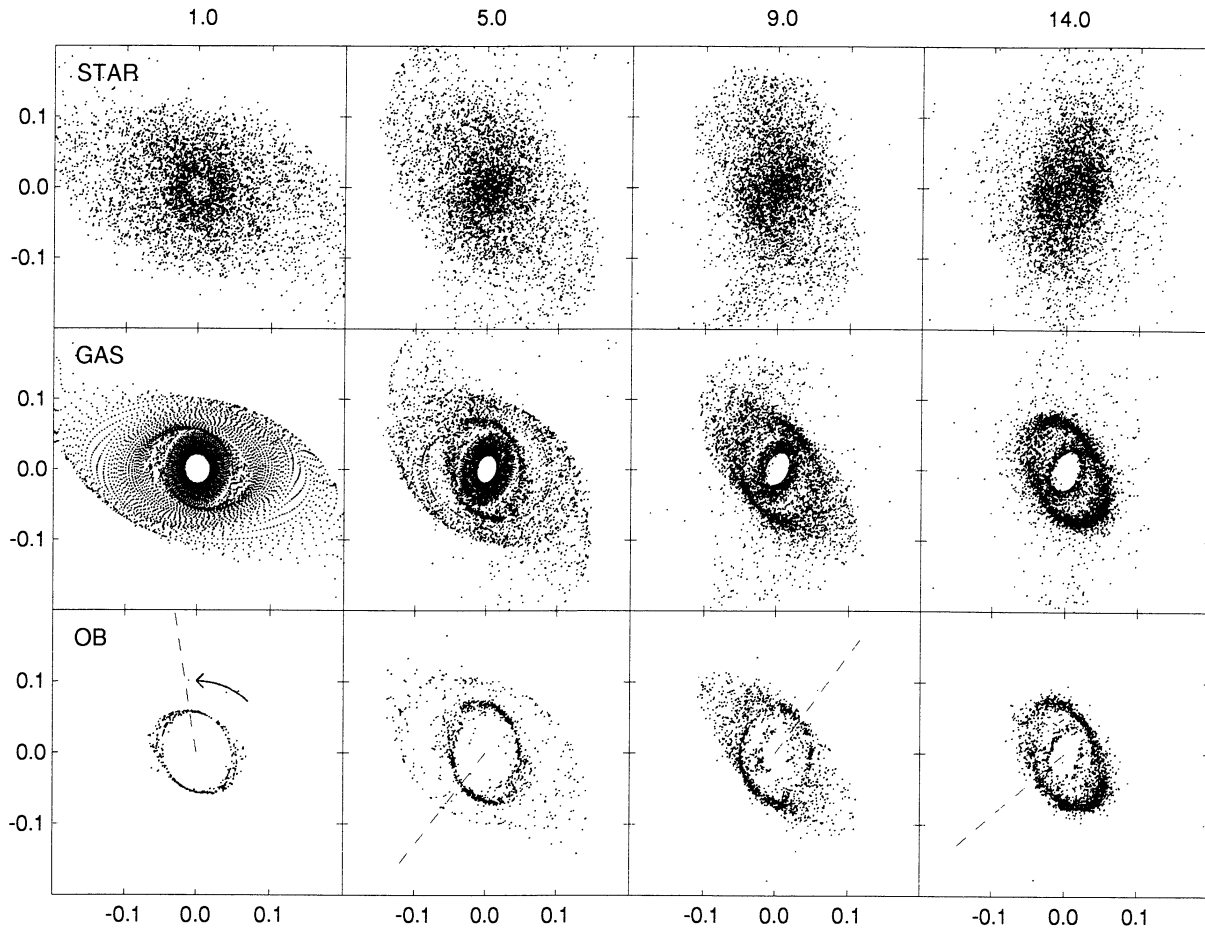
FIG. 15*a*

FIG. 15.—(*a*) Evolution of the companion in an experiment where the potential resolution was improved by a factor of 5 around the companion while the main system was replaced by an analytical halo potential. The companion disk consisted of 30,000 stellar particles and 10,000 colliding gas particles ($\sigma = 0.0025$, $\alpha = 0.1$, $\beta = 0$). Both components had initially the same exponential distribution with $R_e = 0.04$, $R_d = 0.2$. In this experiment the northern side of the companion was assumed to be closer to viewer (*ori* = 1), yielding a relative inclination of 40° as compared with the plane of the main disk. The time evolution of the stellar, gas, and OB particle distributions is displayed, projected to the initial companion plane. In the OB plots, direction of rotation is indicated (*curved arrow*), as well as the projected direction to the main system (*dashed lines*). (*b*) As in (*a*), except that the orientation with the southern side closer to observer is studied (*ori* = 2). This yields a relative inclination of 82° as compared with the plane of the main disk.

the other choice the companion experiences an almost 90° inclined passage of the main system, leading to much weaker direct tidal damage of the outer portions. The later evolution is more similar, leading to strong oval distortion and accumulation of gas into two ring structures, the relative size and orientation depending on the perturbation geometry. Also, in both cases the gas cloud impacts and the formation of OB particles is strongly concentrated on the inner ring structures. During the course of the simulation, the formation rate of OB particles increases continuously and exceeds the nonperturbed value at least by a factor of 5 (compare with a 40% increase for the main system). The rings show quite complicated morphology (for example, they are mutually tilted), and, as their evolution depends on the interplay of several factors (external resonance forcing from the main system, influence of oval deformation of the companion itself), their detailed study is left to future investigation, also taking into account the gas self-gravity. Also, the disk component of the main system should be included in more detailed study, as it will exert torque on the companion. In any case, the location of the rings agrees fairly well with the 2:1 ILR for the external perturbation, as suggested by the simula-

tions of Combes (1988): at the most recent disk crossing, the orbital angular velocity is about 0.85, which equals $\Omega - \kappa/2$, calculated from the initial rotation curve of the companion, at the distance of 0.07 simulation units.

In Figure 16 the projected outlook of the companion to the sky plane is compared for the two orientations. The latter orientation seems to give a better resemblance as compared with the NGC 7752 system, where the faint outer isophotes exhibit a smaller position angle than the bright inner star formation region. Notice, however, that according to Figure 15 the perturbation deforms the companion shape and tilts its plane so strongly that estimating the "original" disk plane from presently observed orientations is not very accurate. Nevertheless, the model with *ori* = 2 leads to quite satisfactory agreement with the observed morphology. For example, the scale of the region of strong OB particle formation is roughly consistent with the bright Hα emission distribution presented by Marcelin et al. (1987). Also, the fact that gas accumulates to rings in the experiments prevents the gas inflow to nuclear regions and is thus consistent with the lack of strong nuclear activity in NGC 7752. The fact that no clear rings are seen in
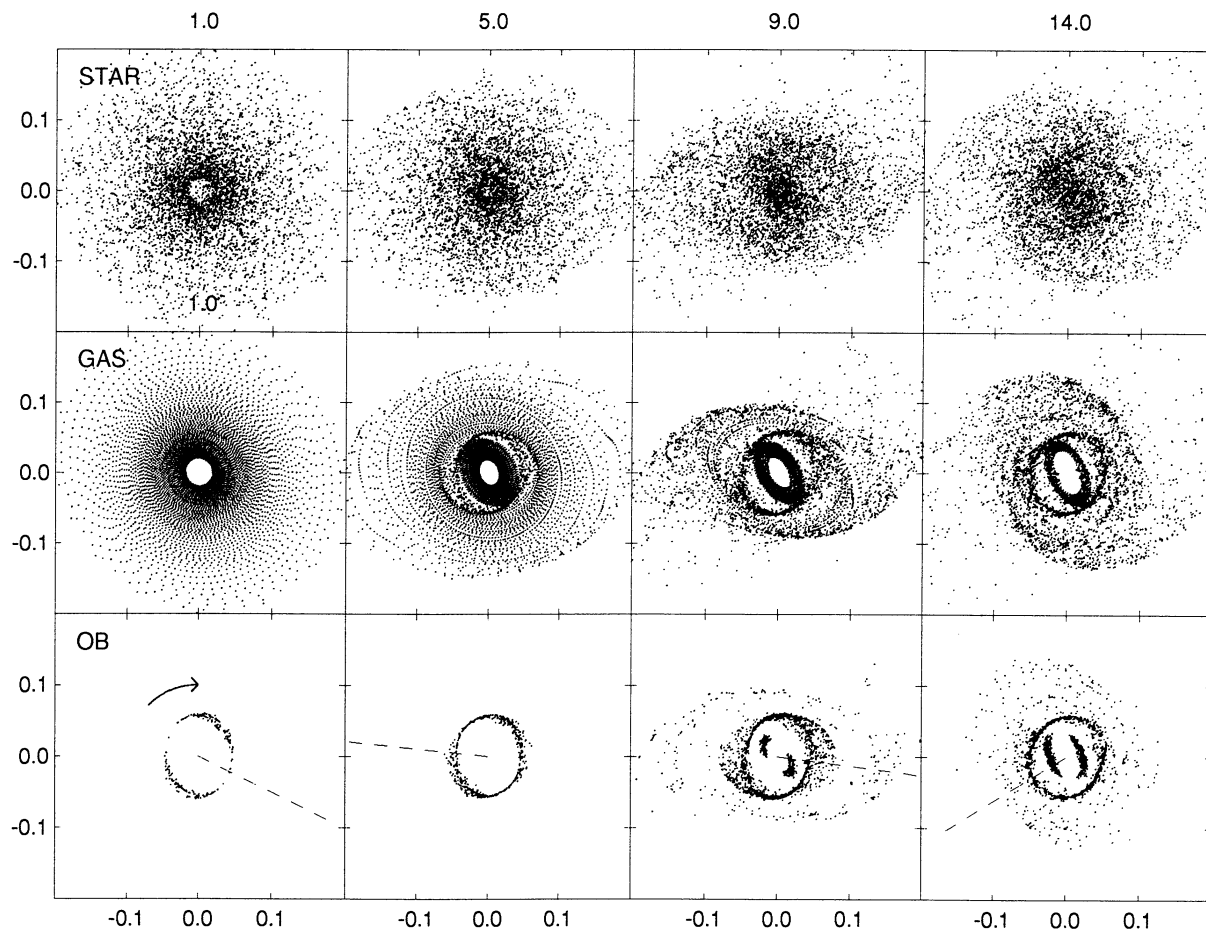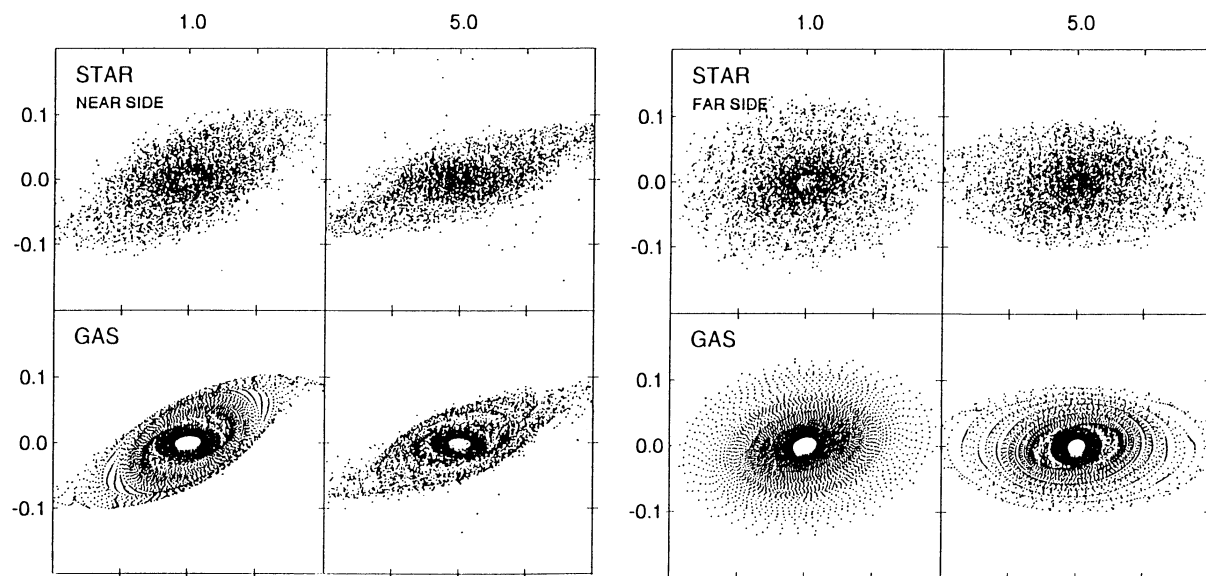
FIG. 15b

FIG. 16.—Projection to the sky plane shown for selected frames of Fig. 15

the observed Hα might be due to limited resolution or, as will be suggested below, to the influence of gas flowing from the main disk, disturbing the ring structures.

In several experiments of the previous sections, it was clearly visible how some fraction of the particles from the main disk ended up in the vicinity of the companion. However, especially for the stellar component, the apparent capture might be just temporary trapping to the vicinity of the companion. Moreover, it might also be overemphasized due to projection effects. On the other hand, the dissipative gas component is expected to behave in a stickier manner, the collisions between gas clouds enabling the true capture. This was verified with experiments where colliding gas is included in both components. The actual amount of transfer is quite sensitive to the distribution of gas in the outer portions of the main disk.

In order to estimate the amount of mass transfer for different initial gas distributions, we studied separately what fraction of particles is being captured from a given initial zone in the main disk, as a function of encounter age. In this manner, we can construct the capture probability $f_{capt}(R, T)$. The total fraction of gas being transferred to the companion then depends on the initial gas distribution $\Sigma(R)$ of the main disk,

$$F_{capt}(T) = \int \Sigma(R) f_{capt}(R, T) R \, dR / \int \Sigma(R) R \, dR . \quad (7)$$

Similarly, the amount of escaped particles $f_{esc}(R, T)$ and $F_{esc}(T)$ can be estimated. The capture and escape fractions were determined from a run where both galaxies were covered by uniform gas disks, extending initially to 1.5 and 0.3 simulation units. This emphasizes the outer regions, so that the calculated probabilities are more accurate. An example is shown in Figure 17, displaying the fate of particles belonging to different initial annuli, for $T = 6$. For $R < 0.6$ practically all particles remain in the disk, while particles with $0.6 < R < 0.8$ form the bridge and tail structures. However, for $R > 0.9$ an increasing fraction of particles either becomes captured to the companion or ends up in rapidly expanding tail structures.

The time variations of $f_{esc}(R, T)$ and $F_{esc}(T)$ are shown in Figures 18a and 18b. The exact numbers obtained depend on the way captured and escaped particles are defined: in Figure 18 rather conservative definitions were used for counting particles as being escaped or captured (see the legend of Fig. 18), which, however, agree well with the visual impression of Figure 17. For example, capture probability seems to be largest for $R \approx 0.9$–1, while for larger distances escape becomes more and more probable. Figures 18c and 18d give the total fraction of escaped and captured particles, calculated according to equation (7) for three different model mass distributions. Case I assumes that the initial gas distribution of the main disk was similar to its stellar distribution (exponential, with $R_e = 0.2$, $R_d = 1.0$). This case, yielding $F_{capt} \sim 0.01$–0.02, can be considered a lower limit, since the gas most probably exhibits a more extended distribution than the stars. On the other hand, case II in Figure 18c represents a definite upper limit, giving the capture probability for a disk extending to 1.5 with uniform density. Finally, case III might be a quite realistic estimate, being based on an exponential gas disk with $R_e = 0.3$, $R_d =$
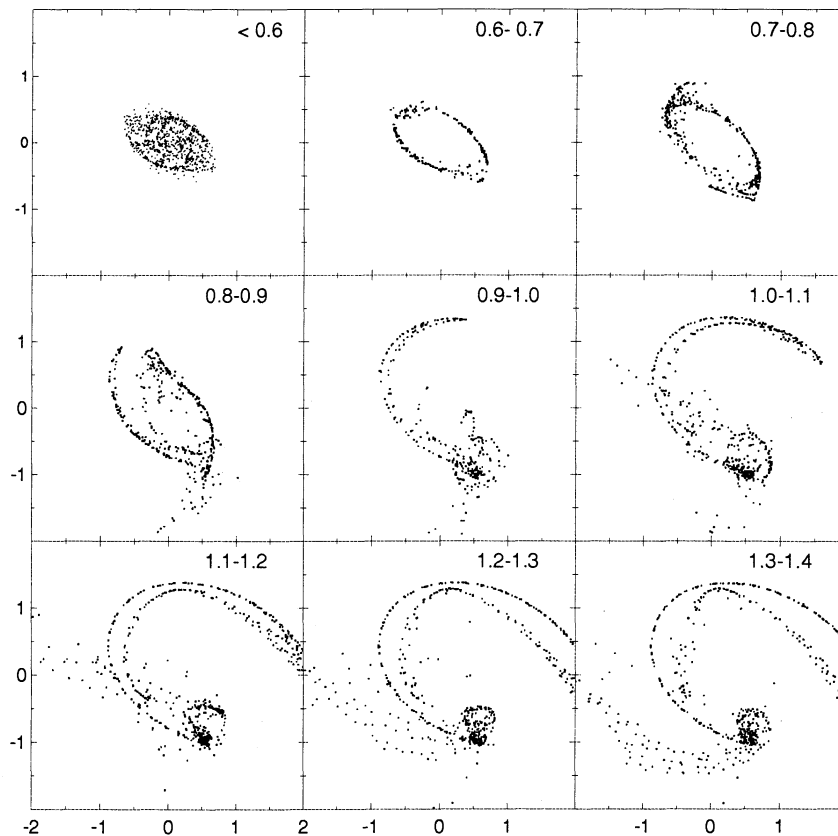

Fig. 17.—Distribution of the main galaxy gas particles after the first half-orbit, shown separately for particles originating from various initial distances. Simulation with nongravitating, collisional gas disks (uniform distribution of particles extending to $R = 1.5$ and $R = 0.3$, around the main system and the companion, respectively). The stellar component was described with the standard gravitating exponential disk.
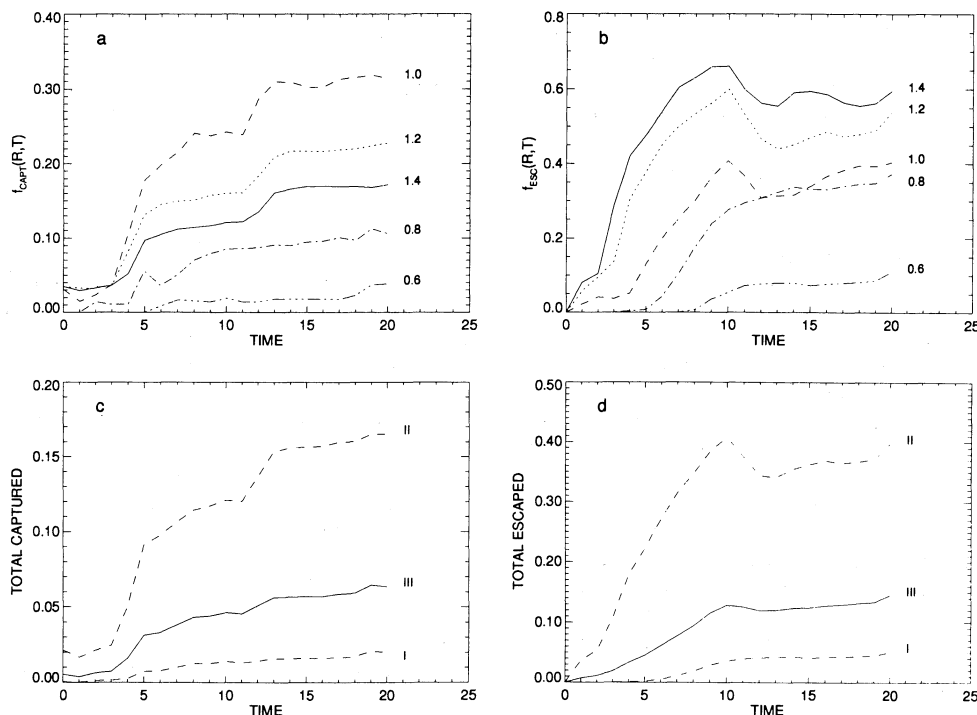
Fig. 18.—Fraction of particles "escaping" the main system (b), as well as those "captured" by the companion (a), shown separately for particles originating from various initial annuli around the nucleus of the primary. Escaped particles are defined as either having positive energy with respect to both components or as having distance larger than 1.5. A particle is defined as captured if it is bound to the companion and not bound to the main system, and is moreover located within $R < 0.2$ from the nucleus of the companion. These data were obtained from a simulation where both components had uniform gas disks extending to 1.5 and 0.3 simulation units, for the main galaxy and the companion, respectively (plus standard exponential stellar disks). Also shown are the total fractions of captured (c) and escaped (d) particles. Estimates for three different initial gas distributions are given in the manner described in text.

1.5. In this case, a total of about 5% of the main galaxy gas mass can have been transferred to the companion (see Fig. 18c at $T \approx 15$, corresponding to two orbital revolutions; at $T = 5$, $F_{capt} \approx 3\%$). For the total amount of escaped material, the case III estimate is about 12%–15%. We also used a similar method to estimate the amount of material escaping from the companion. For all plausible distributions relative escape fractions below 10% were obtained, being thus quite insignificant as compared with mass flow to the companion. Also, by using the above definition for the capture from the main disk, for a nondissipative component (stars), F_{capt} is less by a factor of 10 at least. This follows from the inability of stars to concentrate on the inner regions of the companion, even if they were temporarily in its vicinity.

The above-obtained numbers are to some extent dependent on the size assigned to the companion. However, experiments with moderately reduced R_d for the companion indicate that differences are small. Also, we can argue that in reality even the low surface portions of the disks are strongly affected in the penetrating impact of two disks. In simulations where the fractional surface area covered by particles is small (typically less than 0.01), it is easier for discrete gas clouds to miss mutual collisions. Also, the companion disk orientation was not important for the amount of mass transfer, probably because of the large scatter of material spilled from the main disk.

It is interesting to compare these numbers with the observed neutral gas mass estimates for NGC 7752 and NGC 7753 (see Paper I). The companion is an extremely gas-rich galaxy, having about 1.7 times larger gas–to–total-mass ratio than is typical for normal or starburst galaxies, whereas NGC 7753

has normal or slightly reduced neutral gas content. This could quite naturally be explained by the above-estimated material transfer and escape. For example, assuming that the original NGC 7752 gas content was near normal, even 7%–12% gas flow from the main galaxy to the companion would approximately double the gas content of the companion. However, in Paper I it was estimated that at the present rate of star formation the starburst in NGC 7752 would exhaust its gas content in about 220 Myr, corresponding to only about 25% of our estimated orbital period. Therefore, it appears that the consumption rate is much higher than the supply by material transfer can provide. However, according to Figure 18c, the flow of fresh material to the companion is strongest near the time $T = 5$ when the companion makes an upward crossing with respect to the plane of the main galaxy. Material flow at this instant is stronger than at any other moment studied, because the bridge is in almost physical contact with the companion. Therefore, we probably are now witnessing a particularly active instant in the life of the companion. On the other hand, the activity of the companion might be periodically enhanced always when the companion makes an upward crossing with respect to the plane of the main galaxy (see Fig. 18c, $T = 13$), and once the gas density has exceeded the critical density after the starburst.

Finally, in order to estimate the possible effects of transfer on the companion morphology and activity level, experiments similar to Figure 16b were performed, now including gas also in the main disk. In order to be able to retain the right ratio between the amounts of gas in the two systems, the number of gas clouds in the companion was reduced to 2500. By assuming

that the total mass ratio 0.1 holds also for the initial gas components, this would imply a 10-fold increase in the number of gas particles in the main disk. However, to speed up calculations, only outer zones of the large disk were populated, as the mass transfer from the inner regions is insignificant. The chosen numbers, 10,000 particles in an exponential disk from $R = 0.8$ to $R = 1.2$, with $R_e = 0.3$, should yield approximately the same mass transfer rate as a larger disk between $R = 0$ and $R = 1.5$. A comparison run without mass flow was also performed, verifying that the formation of ring structures is not affected by a reduction in the number of gas clouds.

Figure 19 compares the projected outlook of the companion for two different times ($T = 9$, $T = 14$), with and without mass flow. As seen, mass transfer modifies the regular ring structure into a clumpier distribution, probably as a result of relatively high-speed impacts between clouds originating from different systems. However, the averaged radial distribution of OB particles is almost unaffected, and the scale of the OB particle concentrations is still in good agreement with the observed bright portion of the companion. Notice that we have displayed the system at slightly later times than the present, to give time for the ring structures to form. This accounts qualitatively for the perturbative effects during the previous orbital revolutions at larger relative orbits.

The overall change of the companion activity (OB formation rate) is about twofold during the peak mass transfer period ($T < 10$). At later stages, the collision rate is slightly reduced in the mass flow run, probably because the regular ring-shaped

density enhancements are weaker. Notice, however, that the simulation does not take into account the reduction of the gas content due to star formation: in a true system the observed starburst can be expected to be stronger, and more long-lived, as new material is continuously available as a result of mass transfer.

4. DISCUSSION AND SUMMARY

A reasonably thorough investigation of the possible encounter histories of Arp 86 system has been performed with self-gravitating N-body simulations. The requirement of reproducing the strong inner spiral stucture simultaneously with the outer tidal features, combined with the observational constraints set by the relative position and radial velocity difference, favors a low-inclination, small-eccentricity relative orbit. In particular, parabolic or even near-parabolic orbits are ruled out, because they would indicate very short duration since the principal perturbation and thus are unable to excite the density waves in the inner portions of the NGC 7753 disk. The original Toomre & Toomre (1972) model for the M51 system, based on near-parabolic passage between the systems and short duration since the strongest perturbation, suffers from the same defect, as pointed out by Hernquist (1990) and by Howard & Byrd (1990).

With initial galaxy models where the shape of the mass distribution and the rotation curve was based directly on observations, an orbit was found which could reproduce fairly
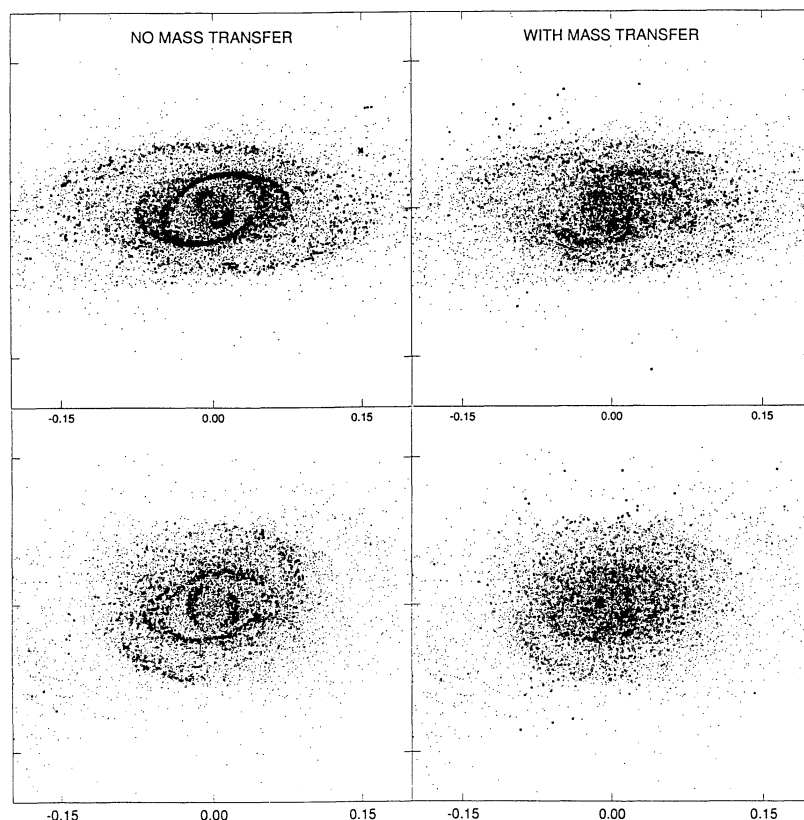

FIG. 19.—Comparison of the projected outlook of the companion in runs without and with material transfer. Distribution of stars (*dots*) and OB particles (*small squares*) is shown for $T = 9$ and $T = 14$. The data at left are from the simulation of Fig. 15*b*. At right, 10,000 gas particles were included in the main disk, in the zone from 0.8–1.2 (exponential distribution with $r_e = 0.3$), whereas the companion had 2500 particles.

accurately the location and shape of both inner and outer spiral arms, as well as the velocity field and major-axis rotation curve measured by Marcelin et al. (1987). This orbit, with 20° inclination with respect to the NGC 7753 disk plane, implies that the bridge in the vicinity of the companion recently moving toward us is originally due to perturbation occurring at approximately the opposite side of the galaxy, while the companion passed *downward* through the NGC 7753 plane, at the distance of ≈7.5 exponential scale lengths. The period of this orbit can be estimated to be approximately 800–900 Myr. Notice that the use of self-gravitating particles was essential in the orbital study, because the inner density-wave structure and strength were the main evidence for the long elapsed time since the principal perturbation. Also, accurate matching of relative velocity and separation constraints were essential in confining the possible orbital parameter space.

This rather interesting orbital configuration is most probably due to dynamical friction that has circularized the initially wider, perhaps only marginally bound orbit. A similar suggestion concerning M51 was recently proposed by Howard & Byrd (1990). The shrinking of the relative orbit was qualitatively verified by studying the future evolution of the orbit, which should lead to merging within 4–5 revolutions. This is an upper bound, as the simulation method does not allow halo deformations and the transfer of orbital energy to halo components is thus not included. On the other hand, the initial decay of the orbit, which would be very sensitive to the extent of the halo (see Barnes 1988), was not addressed. In any case, the suggested orbital geometry implies several previous passages, although weaker than the most recent one. The effects of these previous passages were investigated in a qualitative manner, by studying the stronger changes at future passages. It was found that the system should retain its general morphology during several passages, thus indicating that the fit of the present orbit, based on the perturbations exerted during approximately $\frac{3}{4}$ orbital period, is meaningful. Also, direct observational evidence was found supporting the closed-orbit model—for example, the irregularities in the tail structure at low surface brightness levels. Also, the major-axis rotation curve deforms at successive revolutions in a manner consistent with observations.

Perhaps the most interesting finding concerning the perturbation by the companion at closed orbit involving multiple passages is the general tendency of the main disk to exhibit open spiral structure. Also, the bridge and tail structures tend to be directed along the companion, causing the system to resemble an M51-type object at practically every instant of time. Indeed, if we compare the long-term run of Figure 14 with the VV catalog of M51-type systems (Vorontsov-Vel'yaminov 1976), a counterpart can be found for almost every instant of time. It is very tempting to suggest that the large number of known M51-type systems is not just due to selection effects but that many of them represent objects similar to Arp 86, moving at almost circular relative orbits, rather than being examples of single passages observed at precisely the right instant of time. For example, this would also be the case for Arp 86, if the near-parabolic model of Figure 2 were accepted, with the apparent location of the companion at the tip of the bridge being mere fortuitous coincidence involving our observing direction.

We also addressed the star formation history of NGC 7753, with simulations including dissipatively colliding gas components. Gas compression was found to be initially strongest

at the bridge arm around the first plane crossing, whereas the tail soon starts to dominate. Because of our almost circular orbit, the companion catches the bridge arm again, near its periapse, thus inducing a secondary compression in the bridge it created earlier. This kind of behavior has important implications for the colors of the spiral arms of the main galaxy. Since the bridge has been perturbed longer than the tail, more star formation is induced in the bridge. The strong compression of the bridge during the latest encounter about 50 Myr ago has had time to induce the extreme blue $B - V$ color at the end of the bridge, whereas the $V - R$ gradient might rather be an indication of aging stars, formed during previous interaction history. Although it is not certain whether the simple global gravitational collapse criteria (Kennicutt 1989) holds for local, externally perturbed regions, we suggest that the color gradient and the very blue color $B - V = 0.2$–0.4 at the end of the bridge might be induced principally by local gravitational instabilities leading to growth of molecular cloud complexes and subsequent star formation, as the threshold density for the onset of instability is lowered at large distances owing to weakened differential rotation. Interestingly, Mirabel, Dottori, & Lutz (1992) have recently given evidence for strong ongoing star formation at the tip of the tail in the Antennae system, in a rather low gas density environment.

The tidal arms in our simulations show material wave behavior, whereas the inner parts of the arms are density waves. This density-wave character is suggested to be the reason why spurlike stellar condensations are associated only with the inner portions of the arms: material condensations formed in the arm move with higher angular velocity than the arm itself, and once they have separated from the arm, differential rotation leads to elongated shapes. In simulations, the formation of local gravitational condensations is partially suppressed by limited grid resolution, but its effects were mimicked by strong dissipation in cloud-cloud impacts. The spurs seen in Arp 86 (as well as in many other similar systems, including the much stronger spurs in M51) could also be affected by density perturbations of Julian-Toomre (1966) type in the vicinity of mass concentrations. Rather than being produced by orbiting massive clouds themselves, the excitation could be due to enhanced density in density-wave compression regions. This would naturally explain why spurs extend only outward, although Julian-Toomre models yield a bisymmetric density response: if the perturbation is due to local perturbation moving with the pattern speed of a density wave, its angular velocity matches more closely the material angular speed at a larger radial distance than in the smaller distance, thus breaking the symmetry in the case of orbiting material condensation.

In the material arms the observed star formation either is concentrated to the concave edge of the arms or, as at the double bridge near the companion, shows a very clumpy appearance. On the other hand, at the density-wave region the star formation is distributed over the whole arm widths. This is to some degree opposite to the generally found tendency of star formation to be concentrated on the inner side of density waves, where gas entering the arm feels the strongest compression. The observed smooth distribution might thus indicate that, for example, the strength of the density wave affects the location of preferred star formation. On the other hand, simulations indicate that also in the region of the outer, predominantly material-type arms, there are signs of compression regions moving at different speeds (see, for example, Fig. 6): the

observed string of star formation in the Arp 86 bridge could manifest such waves.

The structure of the companion was studied in detail in runs with increased potential resolution at its disk. At the linearly rising portion of the rotation curve, ring-shaped gas concentrations were obtained, probably due to resonance forcing by the external perturbation. However, since the gas behavior is also altered by the ovally deformed stellar component of the companion, the overall picture is quite complicated and is left to future investigation. As there are two possible true orientations of the companion allowed by its projected orientation, separate simulations were performed to distinguish between them. Based on the apparent warping of the outer parts of the companion, the simulation model with southern side closer to the observer was favored (corresponding to about 80° tilt with respect to the plane of the main disk). However, during the interaction the companion plane is significantly tilted, and therefore its present orientation does not constrain its initial plane very accurately.

The obtained orbital geometry favors mass transfer between systems, especially during the present time when the companion is near the plane of the main disk, and also near the pericenter at the relative orbit. If the mass transfer was included in the simulations, the regular gas ring structure became clumpier and the overall distribution of gas was slightly more centrally concentrated. However, no inflow to nuclear regions was obtained, the gas being trapped at the ring structures. This is consistent with the observed lack of a strong central source. The amount of gas transferred to the companion was estimated to be around 5% of the main disk total gas mass, which is significant as compared with the total gas mass in the companion. This gas transfer, the flow rate being strongest in the near past, is proposed to be the cause of the observed extremely strong starburst, which without a fresh supply of gas should consume all the gas in the companion in about 220 Myr.

5. CONCLUSIONS

The main conclusions of the present study are the following:

1. Based on observed morphology and other observational constraints, the components of Arp 86 are presently moving in a low-eccentricity ($R_{min} = 29$ kpc, $R_{max} = 38$ kpc), low-inclination (20°) orbit. The principal perturbation occurred about 600 Myr ago, as the companion passed below the plane of the main galactic disk at almost opposite direction to its present relative location. The most recent upward crossing occurred about 50 Myr ago.

2. Several M51-type spirals might represent the same kind of system with bound orbits, rather than nonbound passages observed at precisely the correct time. This is supported by the fact that the system shows M51-type structure over several revolutions.

3. The orbit found represents an intermediate phase of its orbital evolution governed by dynamical friction, starting from perhaps only a marginally bound orbit and leading to complete merging. The time scale of this intermediate phase is, however, quite long for the low-mass companion, of the order of several orbital revolutions.

4. About 5% of the main galaxy gas mass can be transferred to the companion during the interaction. This mass flow is proposed to be the cause of the observed starburst. Captured gas as well as the original gas of the companion becomes trapped in the inner ring structures. The clumpy structure obtained in the simulation is in agreement with observations.

This study demonstrates the need of accurate observations for detailed modeling of individual pairs, as well as the importance of using truly self-gravitating methods. In the future, similar studies will be performed for other interacting disk pairs, in order to tackle the dependence between tidal encounters and the different forms of activity induced.

REFERENCES

Barnes, J. E. 1988, AJ, 331, 699
Barnes, J., & Hut, P. 1986, Nature, 324, 446
Binney, J., & Tremaine, S. 1987, in Galactic Dynamics (Princeton: Princeton Univ. Press)
Borne, K. D., & Richstone, D. O. 1991, ApJ, 369, 111
Bushouse, H. A. 1987, ApJ, 326, 49
Combes, F. 1988, in Galactic and Extragalactic Star Formation, ed. R. E. Pudritz & M. Fich (Dordrecht: Kluwer), 475
Combes, F., & Gerin, M. 1985, A&A, 150, 327
Cutri, R. M., & McAlary, C. W. 1985, ApJ, 296, 90
Dahari, O. 1984, AJ, 89, 966
———. 1985, ApJ, 57, 643
Elmegreen, D. M., Elmegreen, B. G., Combes, F., & Bellin, A. D. 1992, A&A, 257, 17
Engström, S., & Athanassoula, L. 1991, in Dynamics of Disk Galaxies, ed. B. Sundelius (Göteborg: Göteborg University and Chalmers University of Technology), 215
Hernquist, L. 1990, in Dynamics and Interactions of Galaxies, ed. R. Wielen (Berlin and Heidelberg: Springer-Verlag), 108
Howard, S., & Byrd, G. 1990, AJ, 99, 1978
Hunter, J. H., Ball, R., & Gottesman, S. T. 1984, MNRAS, 208, 1
Jablonka, J., & Arimoto, N. 1992, A&A, 255, 63
Joseph, R. D., Meikle, W. P. S., Robertson, N. A., & Wright, G. S. 1984, MNRAS, 209, 111
Joseph, R. D., & Wright, G. S. 1985, MNRAS, 214, 87
Julian, W. H., & Toomre, A. 1966, ApJ, 146, 810
Kennicutt, R. C. 1989, ApJ, 344, 685
Kennicutt, R. C., & Keel, W. C. 1984, ApJ, 279, L5
Larson, R. B. 1988, in Galactic and Extragalactic Star Formation, ed. R. E. Pudritz & M. Fich (Dordrecht: Kluwer), 459

Laurikainen, E., & Moles, M. 1989, ApJ, 345, 176
Laurikainen, E., Salo, H., & Aparicio, A. 1993, ApJ, 410, 574 (Paper I)
Marcelin, M., Lecoarer, E., Boulesteix, J., Georgelin, Y., & Monnet, G. 1987, A&A, 179, 101
Mirabel, I. F., Dottori, H., & Lutz, D. 1992, A&A, 256, L19
Noguchi, M. 1988, A&A, 203, 259
Ostriker, J. P., & Peebles, P. J. E. 1973, ApJ, 186, 467
Persic, M., & Salucci, P. 1990, MNRAS, 245, 577
Roberts, W. W., & Haussman, M. A. 1984, ApJ, 237, 404
Salo, H. 1987, Icarus, 70, 37
———. 1991, A&A, 243, 118
———. 1992, Nature, 359, 619
———. 1993, in preparation
Salo, H., & Byrd, G. 1990, BAAS, 22, 951
Schombert, J. M., Wallin, J. F., & Struck-Marcell, C. 1990, AJ, 99, 497
Sellwood, J. A. 1985, MNRAS, 217, 127
Smith, B. J., & Wallin, J. F. 1992, ApJ, 393, 544
Sundelius, B., Thomasson, M., Valtonen, M. J., & Byrd, G. G. 1987, A&A, 174, 67
Thomasson, M. 1987, in IAU Colloq. 96, The Few Body Problem, ed. M. Valtonen (Dordrecht: Kluwer), 387
Toomre, A., & Toomre, J. 1972, ApJ, 178, 623
Vorontsov-Vel'yaminov, B. A. 1976, Soviet Astron., 19 (No. 4), 422
Wallin, J. F. 1990, AJ, 100, 1477
Wisdom, J., & Tremaine, S. 1989, AJ, 95, 925
Wright, G. S., Joseph, R. D., Robertson, N. A., James, P. A., & Meikle, W. P. S. 1988, MNRAS, 233, 1